

On the stability of an in-line formation of hydrodynamically interacting flapping plates

Monika Nitsche¹ , Anand U. Oza²  and Michael Siegel² 

¹Department of Mathematics and Statistics, University of New Mexico, Albuquerque, NM 87131, USA

²Department of Mathematics & Center for Applied Mathematics and Statistics, New Jersey Institute of Technology, Newark, NJ 07102, USA

Corresponding authors: Monika Nitsche, nitsche@unm.edu; Anand U. Oza, ozan@njit.edu

(Received 6 October 2024; revised 12 March 2025; accepted 23 April 2025)

The motion of several plates in an inviscid and incompressible fluid is studied numerically using a vortex sheet model. Two to four plates are initially placed in line, separated by a specified distance, and actuated in the vertical direction with a prescribed oscillatory heaving motion. The vertical motion induces the plates' horizontal acceleration due to their self-induced thrust and fluid drag forces. In certain parameter regimes, the plates adopt equilibrium 'schooling modes', wherein they translate at a steady horizontal velocity while maintaining a constant separation distance between them. The separation distances are found to be quantised on the flapping wavelength. As either the number of plates increases or the flapping amplitude decreases, the schooling modes destabilise via oscillations that propagate downstream from the leader and cause collisions between the plates, an instability that is similar to that observed in recent experiments on flapping wings in a water tank (Newbolt *et al.*, 2024, *Nat. Commun.*, vol. 15, 3462). A simple control mechanism is implemented, wherein each plate accelerates or decelerates according to its velocity relative to the plate directly ahead by modulating its own flapping amplitude. This mechanism is shown to successfully stabilise the schooling modes, with remarkable impact on the regularity of the vortex pattern in the wake. Several phenomena observed in the simulations are obtained by a reduced model based on linear thin-aerofoil theory.

Key words: swimming/flying, vortex shedding, vortex dynamics

1. Introduction

There has been considerable interest recently in understanding the hydrodynamic interactions between flapping wings in moderate to high Reynolds number flows,

for which inertial effects are relevant. Apart from scientific curiosity, this interest is motivated by numerous biological and engineering applications. Specifically, understanding why fish swim in schools (Pavlov & Kasumyan 2000) and birds fly in flocks (Bajec & Heppner 2009) has been of long-standing interest to biologists and physicists studying collective behaviour in animal groups. While many studies have investigated how social interactions between fish may mediate schooling behaviour (Tunstrøm *et al.* 2013; Swain, Couzin & Leonard 2015; Jolles *et al.* 2017), the so-called Lighthill conjecture posits that orderly formations in schools may arise passively due to hydrodynamic interactions, instead of requiring active control or decision making (Lighthill 1975). The underlying mechanisms behind flow-induced collective behaviour could have applications to the next generation of biomimetic underwater vehicles, which self-propel using mechanisms inspired by fish locomotion (Triantafyllou, Triantafyllou & Yue 2000; Geder *et al.* 2017).

Field observations of the formations adopted by fish schools are diverse and typically vary between species (Pavlov & Kasumyan 2000). For instance, some fish species (e.g. minnow, bream, saithe, herring) tend to adopt lattice-like schooling formations, while others (e.g. cod) adopt more disordered configurations (Pitcher 1973; Partridge *et al.* 1980). Recent laboratory experiments have revealed that red nose tetra fish may adopt different lattice-like formations when they school (Ashraf *et al.* 2016, 2017). Our paper is concerned with the simplest of these formations, the so-called in-line formation, in which the line connecting the fish is in the swimming direction. Indeed, fish have been observed to swim in linear chains (Gudger 1944), and pairs of goldfish have recently been observed to school in an in-line formation in which the follower beats its tail to synchronise with the oncoming vortices shed by the leader (Li *et al.* 2020). Flying ibises have also been observed to flock in an in-line formation, a statistical analysis of which reveals certain preferred spatial phase relationships between the wingtip paths of successive birds (Portugal *et al.* 2014).

A number of recent papers have investigated the Lighthill conjecture numerically, by simulating the coupled dynamics of bodies with a prescribed time-periodic flapping kinematics (e.g. heaving, pitching or undulating) and the fluid that surrounds them. The motion of the fluid is determined by solving the Navier–Stokes equations with no-slip boundary conditions on the body, and the dynamics of the bodies are evolved through the influence of drag and thrust forces on them. Simulations of pairs of elastic filaments (Zhu, He & Zhang 2014; Dai *et al.* 2018; Park & Sung 2018) and hydrofoils (Lin *et al.* 2020) in two dimensions have shown that when the bodies are free to evolve in the streamwise (x) direction but constrained in the lateral (y) direction, they tend to adopt certain schooling modes, in which their cycle-averaged velocities and separation distance are constant in time. Simulations have also shown that up to eight flexible plates in two dimensions (Peng, Huang & Lu 2018) and two flexible plates in three dimensions (Arranz, Flores & García-Villalba 2022) may execute a variety of stable in-line schooling modes.

The drawback of numerical methods that solve the Navier–Stokes equations directly is that they are typically limited to moderate Reynolds numbers $Re = O(10^2) - O(10^3)$ due to the presence of boundary layers near the bodies that require increasingly refined grids and thus computational time as the Reynolds number is increased progressively. However, schooling fish often operate in relatively high Reynolds number regimes, $Re = O(10^4)$ or higher (Triantafyllou *et al.* 2000), simulations of which have remained elusive. A tractable alternative is a vortex sheet method, in which fluid viscosity is neglected and the Euler equations are solved directly: the bodies are represented as bound vortex sheets, and free vortex sheets are shed from the bodies' sharp trailing

edges (Alben 2009, 2010; Huang, Nitsche & Kanso 2016; Fang *et al.* 2017). Vortex sheet simulations showed that pairs of rigid plates undergoing either heaving or pitching kinematics can adopt stable in-line schooling modes (Fang 2016; Heydari & Kanso 2021). A recent study of larger in-line formations found that the number of wings that could stably school together was limited by hydrodynamic interactions (Heydari, Hang & Kanso 2024). That is, the number of wings in an in-line school could be increased up to a point, after which the last wing would fall behind and be unable to keep up with the school.

Experimental platforms in which collectives of hydrofoils are actuated in a water tank offer a valuable testbed for investigating the hydrodynamic mechanisms that underpin schooling, as they are more controllable and reproducible than biological systems (Becker *et al.* 2015). A study showed that a pair of hydrofoils that executes heaving kinematics adopts stable steady schooling modes that are quantised on the so-called schooling number $S = d/\lambda$, where d is the tail-to-tip distance between the wings, and $\lambda = U/f$ is the wavelength of the flapping motion, U being the translational velocity, and f the flapping frequency. The schooling number measures the spatial phase coherence of the two swimmers: integer values of the schooling number, which were observed in the experiment, correspond to in-phase states in which the pair traces out the same path through space, while half-integer values indicate out-of-phase states. A recent experimental study on larger collectives of hydrofoils showed that increasingly large chains are unstable to flow-induced instabilities termed *flonons*, wherein the horizontal positions of downstream wings begin to oscillate with increasingly large amplitude down the group, and thus cause collisions between the trailing members (Newbolt *et al.* 2024). That study suggests that while hydrodynamic interactions can bind wings into a schooling mode, they can also lead to an instability that breaks the bound mode.

In this paper, we conduct vortex sheet simulations of collectives of in-line heaving plates, with a view to investigating the bound states and flow-induced instabilities that may arise. Care is taken to evaluate the near-singular integrals that arise when a vortex sheet is near a body, which is essential to prevent the vortex sheets from unphysically crossing the bodies (Nitsche 2021). In summary, we observe that the collectives adopt a number of schooling modes, which become more stable as the flapping amplitude is increased progressively. The separation distances between the plates are quantised on the schooling number, in agreement with experiments on heaving hydrofoils in a water tank (Ramananarivo *et al.* 2016; Newbolt *et al.* 2022, 2024). Moreover, as the number of wings is increased, the collective tends to destabilise via an oscillatory instability that propagates downstream from the leader and causes collisions between the followers, a phenomenon that is reminiscent of the *flonons* observed in recent experiments (Newbolt *et al.* 2024). We rationalise these results qualitatively by proposing a reduced model for the dynamics of interacting plates based on the seminal thin-aerofoil theory of Wu (1961). We also demonstrate that a simple control mechanism, wherein each plate adjusts its flapping amplitude according to its velocity relative to the plate directly ahead, mitigates the flow-induced oscillatory instability.

The paper is organised as follows. In § 2, we present the vortex sheet model (§ 2.1), formulae for the thrust and drag forces (§ 2.2), and the numerical method used to solve the model equations (§ 2.3). The numerical results are presented in § 3: specifically, the steady-state motion for one plate (§ 3.1), sample results for more than one plate (§ 3.2), the evolution towards steady schooling states in multi-plate configurations (§ 3.3), the set of all equilibria and their loss of stability (§ 3.4), our proposed stabilisation mechanism (§ 3.5), and the reduced model based on thin-aerofoil theory (§ 3.6). Concluding remarks are given in § 4.

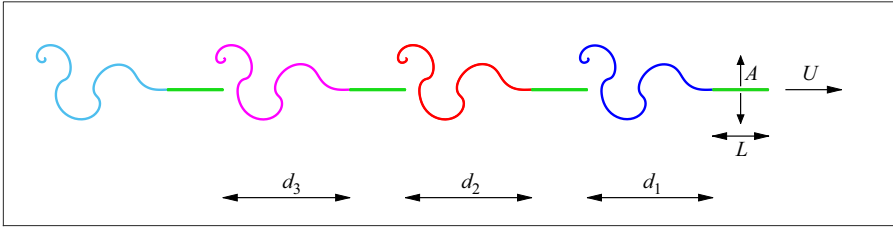


Figure 1. Schematic of the vortex sheet model. The plates (green), each of length L , are in an in-line formation and heave periodically in the vertical direction with amplitude A and frequency f while translating to the right with horizontal velocity U . The vortex sheet shed by the first, second, third or fourth plate is coloured blue, red, pink or cyan, respectively, a colour scheme that will be repeated throughout the text. The figure shows a sample simulation at $t = 3.25$ (which equals 1.625 flapping periods) of $n = 4$ plates with $A = 0.1$ that were initially equispaced by a distance $d_0 = 2.25$. The tail-to-tip distances d_i are also shown.

2. Numerical approach

The model used to simulate n flapping plates is illustrated in [figure 1](#), for $n = 4$. The fluid is assumed to be inviscid and incompressible, and also irrotational except for the wake behind each plate. The wake is modelled by a vortex sheet formed by shedding vorticity from the plates' trailing edges at each time step. The plates are modelled by bound vortex sheets, with vortex sheet strength determined to satisfy the no-penetration boundary condition, or the requirement that no fluid flows through the plates. The fluid velocity in turn is determined by the vorticity in the plates and the wakes.

The plates are all of length L and mass per unit span M , and are constrained to maintain an in-line formation, in that their cycle-averaged positions lie on a single horizontal line. They are initially separated by a distance d_0 from their nearest neighbours, and are given the same initial horizontal velocity U_0 . The prescribed vertical heaving motion is oscillatory with vertical position $A \sin(2\pi ft)$, corresponding to frequency f and amplitude A . This vertical motion induces a horizontal thrust that accelerates the plates, and is countered by a skin friction drag. Thrust and drag forces vary from plate to plate, causing distinct horizontal plate motion and thus distinct evolution of the separation distances $d_j(t)$ between the plates.

While the flow is assumed to be inviscid, viscous effects are accounted for in two ways. First, they are necessary for vorticity to separate from the bodies. Second, they lead to a skin friction drag F_d on each plate, which we model using the Blasius boundary layer drag law $F_d = -C_d \rho \sqrt{L\nu} U^{3/2}$, where C_d is the drag coefficient, ν is the fluid kinematic viscosity, ρ is the fluid density, and U is the instantaneous horizontal velocity of the plate. An alternative drag model used by Fang (2016) and Heydari & Kanso (2021) more closely accounts for the velocity above and below the plate. However, in [Appendix C](#) we present a comparison between these two models, which shows that the differences between them are minor. We thus opt to proceed with the simpler drag model herein. The resulting governing equations of the fluid flow and plates' dynamics is non-dimensionalised by using the plate length L as the length scale, the flapping half-period $1/(2f)$ as the time scale, and $4\rho(Lf)^2$ as the pressure scale. In this paper, we fix the values of the dimensionless plate mass $\tilde{M} = M/\rho L^2$ and drag coefficient $\tilde{C}_d = C_d \sqrt{\nu/(2fL^2)}$, as will be discussed in [§ 3.1](#), and study the dependence of the plate motion on the initial velocity $\tilde{U}_0 = U_0/(2Lf)$, the initial separation distance $\tilde{d}_0 = d_0/L$, the flapping amplitude $\tilde{A} = A/L$, and the number of plates n . From here on, all variables are non-dimensional and the tildes are dropped.

2.1. The vortex sheet model

The n bound vortex sheets representing the flat plates have positions

$$\mathbf{x}_b^j(\alpha, t) = (x_b^j, y_b^j)(\alpha, t), \quad \alpha \in [0, \pi], \quad j = 1, \dots, n, \quad (2.1)$$

and sheet strengths $\gamma^j(\alpha, t)$. The sheets are initially on the horizontal x -axis, with position

$$x_b^j(\alpha, 0) = s(\alpha) - (j-1)(d_0 + 1), \quad s(\alpha) = \cos(\alpha)/2, \quad (2.2)$$

$$y_b^j(\alpha, 0) = 0. \quad (2.3)$$

That is, each plate has unit length, with $\alpha = 0$ at the leading edge (right), $\alpha = \pi$ at the trailing edge (left), and d_0 the tail-to-tip distance between plates. The horizontal evolution of x_b^j is determined by the displacement $X^j(t)$ of plate j from its initial position, while the oscillatory vertical component $y_b^j(t)$ is prescribed:

$$x_b^j(\alpha, t) = X^j(t) + x_b^j(\alpha, 0), \quad X^j(0) = 0 \quad (2.4a)$$

$$y_b^j(\alpha, t) = A \sin(\pi t). \quad (2.4b)$$

The plate position $X^j(t)$ evolves according to the induced thrust and drag forces acting on the plate (see § 2.2). The plate vortex sheet strength is determined numerically by enforcing the no-penetration boundary condition on the plate walls.

The free vortex sheets representing the wakes are parametrised by the circulation parameter Γ , where Γ_T^j is the total circulation around the j th sheet:

$$\mathbf{x}_f^j(\Gamma, t), \quad \Gamma \in [0, \Gamma_T^j], \quad j = 1, \dots, n. \quad (2.5)$$

Together, the free and bound vortex sheets induce the fluid velocity at any point \mathbf{x}_o :

$$\begin{aligned} \mathbf{u}(\mathbf{x}_o, t) = \frac{1}{2\pi} \sum_{j=1}^n \left[\int_0^\pi \frac{(\mathbf{x}_o - \mathbf{x}_b^j(\alpha, t))^\perp}{|\mathbf{x}_o - \mathbf{x}_b^j(\alpha, t)|^2} \gamma^j(\alpha, t) s'(\alpha) d\alpha \right. \\ \left. + \int_0^{\Gamma_T^j} \frac{(\mathbf{x}_o - \mathbf{x}_f^j(\Gamma, t))^\perp}{|\mathbf{x}_o - \mathbf{x}_f^j(\Gamma, t)|^2 + \delta^2} d\Gamma \right], \end{aligned} \quad (2.6)$$

where $(x, y)^\perp = (-y, x)$. Here, the parameter δ regularises the flow for points \mathbf{x}_o near or on the free sheet, using the vortex blob method (Krasny 1986). If \mathbf{x}_o is a point on the plate, then the integrals in (2.6) are evaluated in the principal value sense, and yield the average of the velocity above and below the plate.

The free sheet evolves with the fluid velocity (2.6) as

$$\frac{d\mathbf{x}_f^j}{dt}(\Gamma, t) = \mathbf{u}(\mathbf{x}_f^j(\Gamma, t), t). \quad (2.7)$$

Its circulation Γ is determined using the circulation shedding algorithm of Nitsche & Krasny (1994). Vorticity is shed at time t by releasing a particle from the plate's trailing edge, with vertical velocity equal to the plate's vertical velocity, and horizontal velocity equal to the average horizontal fluid velocity $u(\mathbf{x}^j(\pi, t), t) = \bar{U}_e^j$ at the trailing edge, as obtained from (2.6). The particle's circulation is such that the Kutta condition is satisfied,

with

$$\frac{d\Gamma_T^j}{dt} = -\frac{1}{2}[(u_+^j)^2 - (u_-^j)^2], \quad (2.8a)$$

$$\overline{U}_e^j = \frac{1}{2}(u_+^j + u_-^j), \quad (2.8b)$$

$$\gamma^j(\pi, t) = u_-^j - u_+^j, \quad (2.8c)$$

Here, u_+^j and u_-^j are the horizontal velocity components above and below the j th plate at the trailing edge, obtained from $\gamma^j(\pi, t)$ and \overline{U}_e^j .

2.2. Thrust and drag

The plates experience a thrust force due to the suction at their leading edges, which arises because the fluid velocity is singular there. Specifically, the thrust is obtained from the leading edge bound vortex sheet strength. The sheet strength is unbounded at the leading edge, with $\gamma^j(\alpha, t) \sim \Delta s^{-1/2}$ as $\Delta s \rightarrow 0$, where $\Delta s = 1/2 - s(\alpha)$ is the distance from the leading edge. However, the desingularised vortex sheet strength $\gamma^j(\alpha) s'(\alpha)$ remains bounded. The horizontal thrust force acting on the plate is given by (Fang *et al.* 2017; Eldredge 2019)

$$F_x^j = \frac{\pi}{4} \tilde{\gamma}_j^2, \quad \text{where } \tilde{\gamma}_j = \lim_{s \rightarrow 1/2} \gamma^j(s) \sqrt{\frac{1}{4} - s^2}, \quad (2.9)$$

and, with our choice of $s(\alpha) = \cos \alpha/2$,

$$\tilde{\gamma}_j = - \lim_{\alpha \rightarrow 0} \gamma^j(\alpha) s'(\alpha). \quad (2.10)$$

The relation (2.9) holds for steady or unsteady plate motion. For steady motions, the result reduces to $\tilde{\gamma} = -2V$, where V is the vertical velocity of the leading edge, which is used by Alben (2010). For completeness, both the unsteady and steady results are derived here, in Appendices A and B, respectively. Appendix B also shows a comparison between the flow field around a plate in a steady vertical flow, and the unsteady flow field around an impulsively started plate moving vertically upwards with constant velocity, the latter being computed using the method described in § 2.3. We detail how the flow field (figure 14) and circulation (figure 15) in the unsteady case approach that of the steady case in the long-time limit.

As discussed at the beginning of § 2, the drag force acting on the plate is modelled to be proportional to $(U^j(t))^{3/2}$, where $U^j(t)$ is the plate velocity. The horizontal motion of the n plates is thus governed by the system of ordinary differential equations

$$\frac{dX^j}{dt} = U^j, \quad X^j(0) = 0 \quad (2.11a)$$

$$M \frac{dU^j}{dt} = \frac{\pi}{4} \tilde{\gamma}_j^2 - C_d (U^j)^{3/2}, \quad U^j(0) = U_0. \quad (2.11b)$$

The flow evolution is determined by the system of ordinary differential equations (ODEs) (2.7), (2.8) and (2.11), in addition to a Fredholm integral equation for $\tilde{\gamma}$. Its numerical solution is described next.

2.3. Numerical method

The plates (2.1) are each discretised by $N_b + 1$ point vortices corresponding to $\alpha_k = k\pi/N_b$, $k = 0, \dots, N_b$. The free vortex sheets are discretised by $N_f + 1$ vortex blobs with total circulation Γ_T^j , created by shedding one blob at each time step; thus N_f increases with time. Time is discretised by $t_m = m \Delta t(t)$, where typically Δt is smaller at early times near the beginning of the motion, and increases linearly from Δt_1 to a final time step Δt_2 at a time t_1 , after which it remains constant. The small initial time steps are needed to resolve the large initial velocities about the trailing edge. The system of ODEs (2.7), (2.8) and (2.11) is solved using the fourth-order Runge–Kutta method. At each stage, the following steps are taken (Sheng *et al.* 2012).

- (i) Set the vertical plate velocity $V(t) = A\pi \cos(\pi t)$.
- (ii) For each plate $j = 1, \dots, n$, find the sheet strength $\gamma_k^j = \gamma^j(\alpha_k, t)$ such that the vertical fluid velocity in (2.6) evaluated at the midpoints $\alpha_k^m = (\alpha_{k-1} + \alpha_k)/2$ equals the prescribed vertical plate velocity,

$$\mathbf{u} \left(\mathbf{x}_b^j(\alpha_k^m, t), t \right) \cdot \mathbf{n} = V(t), \quad k = 1, \dots, N_b, \quad (2.12)$$

where $\mathbf{n} = (0, 1)$ is normal to the plate. Here, the singular integrals in the velocity (2.6) are computed with what is in essence the alternating point vortex method of Shelley (1992). In addition, enforce zero total circulation around the plate and its wake. The resulting $(N_b + 1) \times (N_b + 1)$ linear system for γ_k^j , $k = 0, \dots, N_b$, is inverted using a precomputed LU decomposition.

- (iii) Set $\gamma^j(\pi, t) = \gamma_{N_b}^j$ and $\bar{U}_e^j = u(\mathbf{x}_b^j(\alpha_{N_b}^m, t), t)$, and obtain u_j^+ and u_j^- using (2.8b) and (2.8c). Then shed a particle \mathbf{x}_{new}^j from each trailing edge with velocity

$$\frac{d\mathbf{x}_{new}^j}{dt} = (\bar{U}_e^j, V) \quad (2.13)$$

and circulation such that (2.8a) is satisfied. As explained by Nitsche & Krasny (1994, § 2.4(iii)), only separated flow is considered when determining u_j^+ and u_j^- .

- (iv) Move all previously shed particles with velocity

$$\frac{d\mathbf{x}_{f,k}^j}{dt} = \mathbf{u} \left(\mathbf{x}_{f,k}^j, t \right), \quad k = 0, \dots, N_f^j, \quad (2.14)$$

and add $\mathbf{x}_{f,N_f^j+1}^j = \mathbf{x}_{new}^j$, then increase N_f^j by 1. Here, the integral over the bound vortex sheets in (2.6) is near-singular when the target point is near a plate. The near-singular integrals are computed using the corrected trapezoid rule of Nitsche (2021).

- (v) Determine the desingularised leading edge sheet strength $\tilde{\gamma}_j$ using (2.10), and move the plates by (2.11).

Typically, one new particle is shed per time step. In some cases, a particle is shed every other time step or more for the sake of computational efficiency.

3. Numerical results

This section presents numerical results for $n = 1, 2, 3$ and 4 plates, with flapping amplitudes $A = 0.1$ – 0.4 , mass $M = 1$, and drag coefficient $C_d = 0.1$. The numerical parameters are $\delta = 0.2$, $N_b = 100$, $t_1 = 1$, $\Delta t_2 = 0.008/A$ and $\Delta t_1 \approx \Delta t_2/10$.

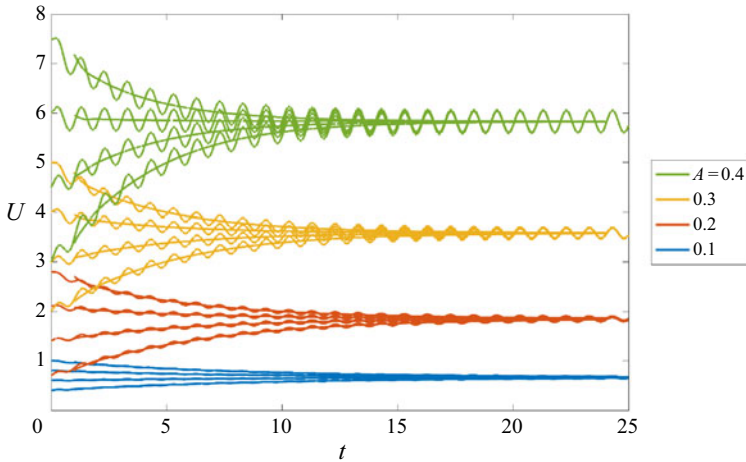


Figure 2. Time evolution of the translation velocity U of a single plate ($n = 1$), for various initial velocities U_0 and the four amplitudes A indicated in the legend. The oscillatory curves show the instantaneous velocity $U(t)$, upon which we have superimposed a cycle-averaged velocity obtained by averaging $U(t)$ over a moving window of size equal to the oscillation period.

Results were confirmed to remain basically unchanged under mesh refinement (decreasing Δt , increasing N_b) or smaller values of δ .

3.1. Single plate, $n = 1$

Here, we consider one plate moving with a prescribed oscillatory heaving motion of amplitude A , given an initial horizontal velocity U_0 . The plate moves forward by the thrust force (2.9), as vorticity is shed from its trailing edge. Figure 2 shows the resulting horizontal plate velocity for a range of amplitudes A and initial velocities U_0 . The plate horizontal velocity oscillates with the same frequency as the heaving motion. For each case, the figure shows both the actual oscillatory velocity $U(t)$, and the cycle-averaged velocity obtained by averaging $U(t)$ over a moving window of size equal to the oscillation period. The figure shows that in all cases, the cycle-averaged plate velocity approaches a steady-state velocity U_∞ that depends solely on the amplitude A and is independent of the initial velocity U_0 . The steady-state velocity U_∞ increases as A increases, with values $U_\infty = 0.665, 1.85, 3.58$ and 5.83 for $A = 0.1, 0.2, 0.3$ and 0.4 , respectively. These values of U_∞ are approximately consistent with those obtained in experiments on heaving wings in a water tank (Ramanananarivo *et al.* 2016), which motivates our choice of the drag coefficient C_d .

Figure 3(a) shows the shed vortex sheet behind one plate oscillating with amplitude $A = 0.2$, at time $t = 25$. The given initial velocity is that of the corresponding steady state, $U_0 = 1.85$. With each upward (downward) motion of the plate, positive (negative) vorticity is shed from the trailing edge, which leads to a sequence of counter-rotating vortex pairs shed during each oscillation period. By taking the curl of (2.6), we obtain the regularised vorticity corresponding to the shed vortex sheet, which is shown in figure 4(a). Soon after being shed, the vorticity settles into a sequence of almost equally spaced vortices of alternating sign, with the positive (negative) vortex positioned slightly below (above) the centreline $y = 0$.

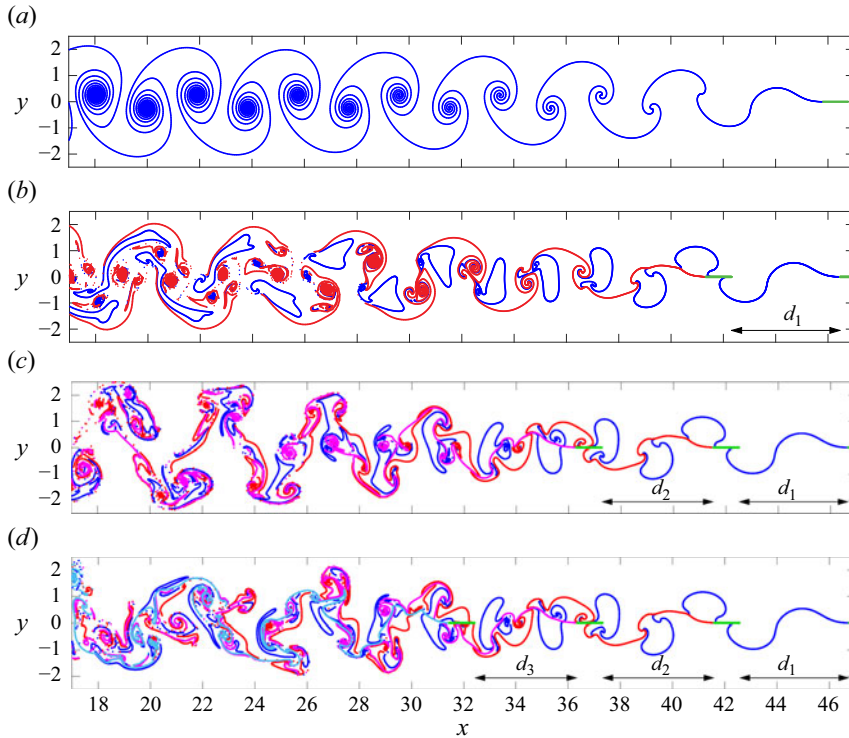


Figure 3. Plate and vortex sheet positions at $t = 25$, for the flapping amplitude $A = 0.2$ and $n = 1, 2, 3$ and 4 plates (from top to bottom). All plates are initially equispaced with a distance near $d_0 = 4.2$.

3.2. Several plates, $n = 2, 3, 4$

Figure 3(b) shows the two vortex sheets shed behind two plates, both heaving with amplitude $A = 0.2$. The colour scheme is the same as that in figure 1, with the vortex sheet shed by the leader (follower) plate indicated in blue (red). There is a large amount of stretching far downstream of the plates as the two sheets interact. We plot the sheets using a linear interpolant of the shed point vortices if neighbouring points are sufficiently close to each other. Otherwise, after a sufficiently large amount of stretching, we simply plot the individual point vortex positions. The initial distance between the plates is $d_0 = 4.2$, which is, as will be seen later, near an equilibrium position. The two sheets are seen to roll up into four vortices per period, a phenomenon that is also evident in the top panel of supplementary movie 1. This is seen more clearly in figure 4(b), which shows a sequence of two positive vortices followed by two negative vortices per period. This pattern repeats, although in an irregular fashion. Groups of four vortices are discernible, but their relative positions do not settle into a clear steady pattern.

Figure 3(c) shows the three vortex sheets shed behind three plates heaving with amplitude $A = 0.2$. The initial separation between all plates is as before, $d_0 = 4.2$. A pattern seems to appear farther downstream of the plates. Most notably, near $x = 20$, the vortices have spread further from the midline $y = 0$. Figure 4(c) reveals more clearly a repeating pattern of groups of six vortices, i.e. three positive followed by three negative. Sufficiently far downstream, for $x < 25$, the vorticity is clearly concentrated away from the midline, as it has spread significantly farther than in the $n = 2$ case shown in figure 4(b). A simulation with $n = 3$ plates is shown in supplementary movie 2.

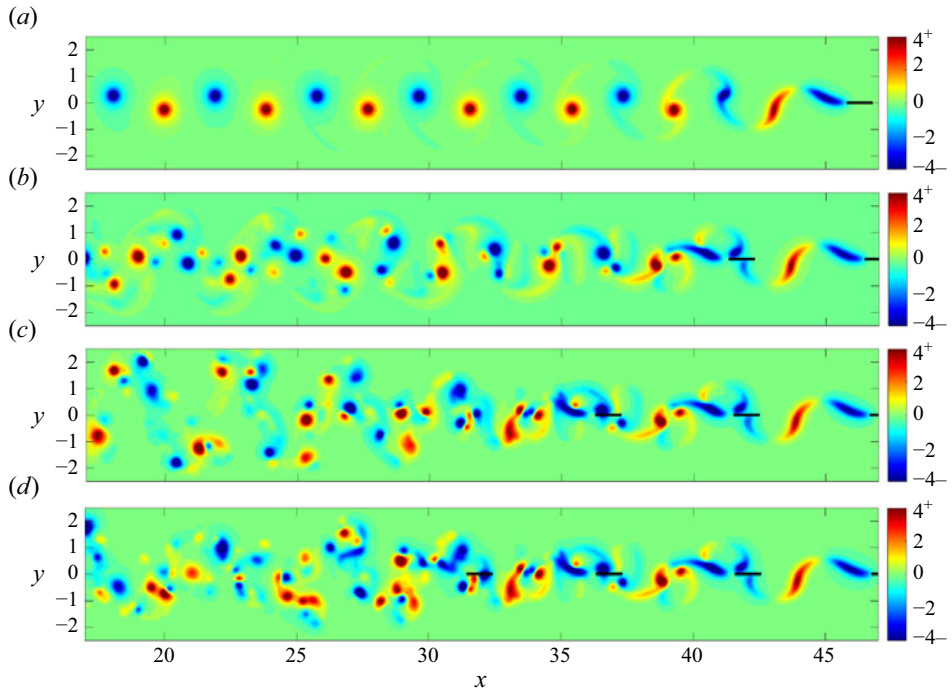


Figure 4. Same as figure 3, but the regularised vorticity is plotted instead of the vortex sheet. The plates are indicated in black. Absolute vorticity values larger than 4 are represented by the darkest blue and red colours.

Figures 3(d) and 4(d) show the vortex sheets and corresponding vorticity shed behind $n = 4$ moving plates. It is difficult to detect a pattern in the downstream vortex sheet positions. The vorticity is expected to consist of groups of eight vortices, i.e. four positive followed by four negative, but the pattern is less clear and more random. Furthermore, the spread away from the midline is not as big as for $n = 3$. A simulation with $n = 4$ plates is shown in supplementary movie 3.

The effect of the trailing plates on the leader is seen most clearly in figure 3. In all four cases, the given initial velocity is $U_0 = 1.85$, and the initial distances between the plates are $d_j(0) = 4.2$. The shape of the sheet between the first and second plates is basically unchanged in all cases from the single-plate case. That is, the second plate has little influence on the wake in front of it. Similarly, the wake behind the second and third plates is unchanged from the $n = 2$ case, so the third plate also has little influence on the wake in front of it. It is evident that as the number of plates behind the front plate increases, the front plate has travelled slightly further by $t = 25$. However, after an initial transient, we observe that U_∞ remains essentially unchanged, with only a small increase of less than 3 % as n increases. We attribute this increase in the leader's velocity, albeit small, to the fact that the leader's bound vorticity is modified by the downstream plates' bound and shed vorticity, as is evident from step (ii) of the numerical method presented in § 2.3. The leader's bound vorticity in turn affects its thrust, as given by (2.9).

3.3. Steady-state positions for $A = 0.2$, $n = 2$

The distances $d_j(t)$ between the plates evolve in time. We are interested in the long-term behaviour of d_j and the associated possible steady-state configurations. This subsection presents results for a pair of wings ($n = 2$) with flapping amplitude $A = 0.2$, with a range of

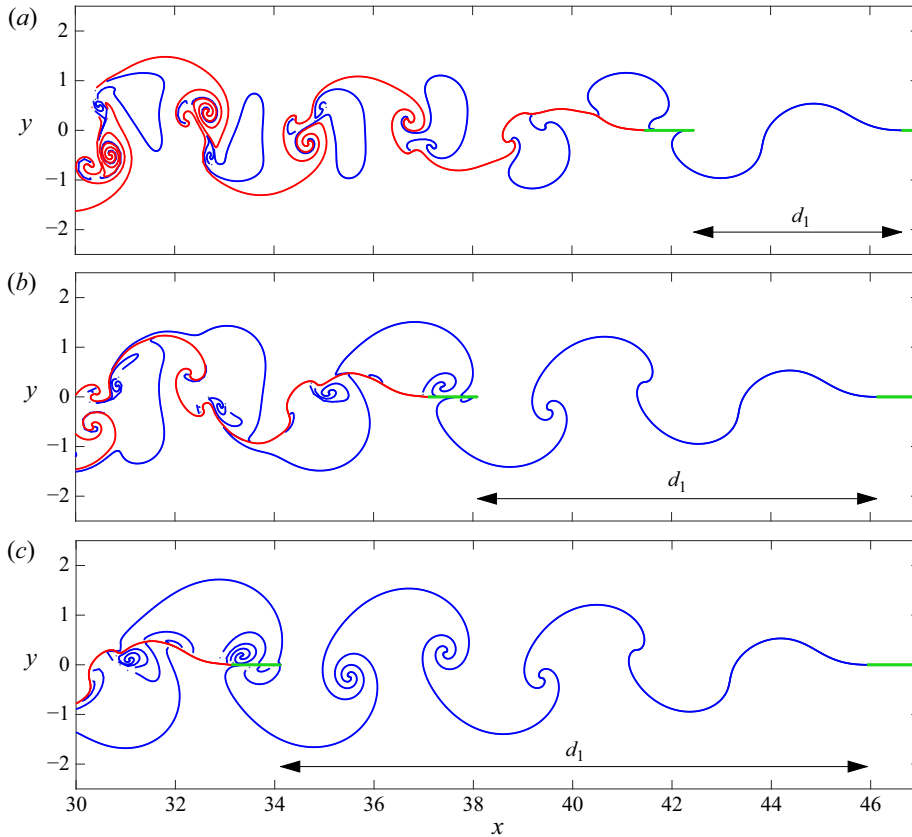


Figure 5. Snapshot at $t = 25$ of three of the schooling modes obtained for a pair of plates ($n = 2$) with flapping amplitude $A = 0.2$. The plates are initially located near the first, second and third equilibria, which, from top to bottom, correspond to the distances $d_1^{\infty,1} = 4.18$, $d_1^{\infty,2} = 8.01$ and $d_1^{\infty,3} = 11.82$, respectively.

initial separation distances d_0 . Since the steady-state cycle-averaged plate velocity U_∞ is found to always be independent of U_0 , from here on, the initial horizontal velocity of each plate is taken to be the steady-state cycle-averaged velocity of a single plate flapping with the same amplitude. We observe that the two plates evolve towards a steady configuration in which the distance between them, after undergoing several oscillations, approaches a constant, but that this equilibrium distance d_1^∞ depends on the initial distance d_0 . Figure 5 shows snapshots of simulations performed for three different values of d_0 , at a time when the separation distance d_1 between the plates has reached the equilibrium values $d_1^{\infty,1}$, $d_1^{\infty,2}$ and $d_1^{\infty,3}$. Supplementary movie 1 also shows examples of simulations performed for different values of d_0 , which illustrates how changing d_0 causes the pair of plates to attain different equilibria.

Note that in figure 5(a), the distance $d_1^{\infty,1}$ between the plates is approximately the distance travelled by the plate in one period of the heaving oscillation, as evident by the single upward and downward wave of the shed sheet. In figure 5(b), the equilibrium distance is approximately twice that of figure 5(a), and in figure 5(c) it is approximately three times. The distance travelled by a plate with velocity U_∞ in one oscillation period is the wavelength $\lambda = U_\infty/f$, where $f = 1/2$. Using the value $U_\infty = 1.85$ corresponding to $A = 0.2$, we find that the equilibrium positions satisfy

$$d_1^{\infty,1} \approx 4.18 \approx 1.13\lambda, \quad d_1^{\infty,2} \approx 8.01 \approx 2.16\lambda \quad \text{and} \quad d_1^{\infty,3} \approx 11.82 \approx 3.19\lambda. \quad (3.1)$$

Clearly, the plates have settled at equilibrium configurations near integer values of the non-dimensional schooling number (Becker *et al.* 2015)

$$S_k = \frac{d_1^{\infty,k}}{\lambda}. \quad (3.2)$$

Note that while the first equilibrium has schooling number $S_1 = 1.13$, i.e. slightly larger than 1, the following schooling numbers $S_2 = 2.16$ and $S_3 = 3.19$ increase approximately by integer values, $S_k \approx S_{k-1} + 1$.

3.4. Equilibrium schooling states and their loss of stability

Figure 6 shows the dependence of the distances $d_j(t)$ between plates on the initial separation distance d_0 , for in-line formations of $n = 2, 3$ and 4 wings (columns from left to right) and the three flapping amplitudes $A = 0.4, 0.3$ and 0.1 (top to bottom rows). These flapping amplitudes complement the value $A = 0.2$ considered in § 3.3. We proceed by discussing each column in turn.

The first column shows results for $n = 2$ plates. It shows the distance $d_1(t)$ between the plates as a function of time, for 35 or 36 different initial separation distances d_0 . During an initial time interval of length approximately d_0/U_∞ , the vorticity of the leader has not yet reached the follower, and both plates travel with the same velocity, each without the influence of the other. During that time interval, the distance between them stays constant. The larger the initial distance d_0 , the longer this initial time interval. Once the vortex wake of the leader reaches the follower, that vorticity changes the evolution of the follower, and the distance between the plates changes. In all cases, the distance $d_1(t)$ initially oscillates, then the amplitude of these oscillations decreases in time as d_1 approaches a constant steady-state value. Notice that the steady-state distances $d_1^{\infty,k}$ decrease in proportion to U_∞ as A decreases from 0.4 (top row) to 0.1 (bottom row). That is, as the heaving amplitude is decreased progressively, the plates are closer together in their steady configurations. Note also that the oscillations in d_1 are larger, relative to the value of d_1 , for smaller values of A .

As already observed in figure 5, there are several steady states, depending on the value of d_0 . The steady states are measured by their schooling number (3.2), using the value for U_∞ corresponding to the given value of A . The distinct values of d_0 yield six distinct corresponding steady states, S_1, \dots, S_6 . The schooling numbers associated with each steady state are listed in black in the first column of figure 6, and the differences between them are in red. For all three values of A , S_1 is slightly larger than 1, with larger schooling numbers increasing by integer values as observed in § 3.3.

The curves are colour-coded according to the steady state reached. The curve with smallest d_0 is black and reaches zero in finite time, which corresponds to collision of the two plates. While generally the leader travels without being influenced much by the follower, the follower may accelerate and collide with the leader if the initial separation distance is sufficiently small.

The second column in figure 6 illustrates the case of $n = 3$ plates, and shows the distance $d_2(t)$ between the second and third plates. As for $n = 2$, the addition of an n th plate behind a group of $n - 1$ plates leaves the motion of the first $n - 1$ plates mostly unchanged. That is, for $n = 3$, the dynamics of $d_1(t)$ is roughly the same as that shown in the first column of figure 6, except in those cases of collision between the second and third plates, after which the computation stops. The curves are coloured by the equilibrium reached in the

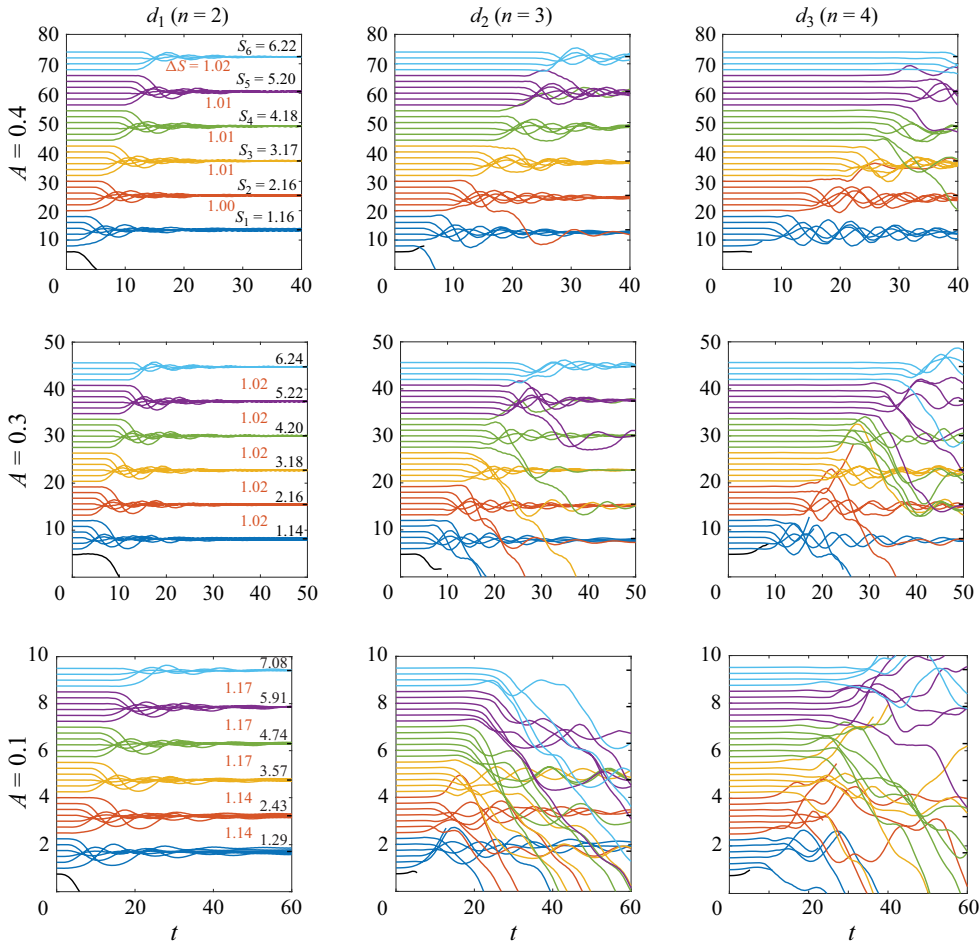


Figure 6. Time evolution of the distances $d_1(t)$ (left-hand column), $d_2(t)$ (middle column) and $d_3(t)$ (right-hand column) for in-line formations of $n=2$, 3 and 4 plates, respectively. The plots in the top, middle and bottom rows correspond to the heaving amplitudes $A=0.4$, 0.3 and 0.1, respectively. The different curves in each plot are obtained by varying the initial distances $d_j(0)$, and are colour-coded according to the equilibrium schooling mode reached for two plates ($n=2$, left-hand column). The schooling numbers $S_k = d_1^{\infty,k} / \lambda$ corresponding to each equilibrium distance $d_1^{\infty,k}$ are written in black in the first column, with the differences between them written in red. Here, $\lambda = 2U_\infty$ is computed using the steady-state U_∞ for the pair of plates.

absence of the third plate, i.e. using the same colour for a given d_0 as in the first column of figure 6.

In the case of $n=3$ plates, the second and third plates move with the same velocity until the vortex wake from the first plate reaches the last plate, since, before then, they both are affected only by the (equal) wake from the plate directly ahead. The time interval of constant d_2 is therefore approximately $2d_0/U_\infty$, twice as long as the time interval of constant d_1 . However, after this interval, the motion is more irregular than in the case of two plates, as is evident by comparing the first and second columns of figure 6. For $A=0.4$ (top row), one trajectory close to S_2 (red) jumps to S_1 . For $A=0.3$ (middle row), there are more trajectories that move to a different, typically lower, equilibrium schooling number. There are also more collisions between the plates. The situation is noticeably worse for

$A = 0.1$ (bottom row). Only a few curves reach their corresponding equilibrium, with the rest either exhibiting collisions or being on the path to collision. We thus conclude that the equilibria S_k appear to lose stability when n is increased from 2 to 3, and when A is decreased from 0.4 to 0.1. We note that some of the curves showing d_2 , e.g. the black curves at the bottom of the panels in the second column, terminate abruptly despite staying strictly positive. This behaviour indicates that the first two plates have collided, while the third has not.

The case of $n = 4$ plates, with d_3 plotted in the third column of [figure 6](#), confirms this pattern. There are more irregular paths for $A = 0.4$ (top row) than there were with $n = 3$, with one, in green, possibly approaching collision. The results for $A = 0.3$ (middle row) show many curves that end at a finite time, corresponding to collisions in d_2 that are shown in the middle column. In addition, there are more collisions and many more curves that leave their original equilibrium. The basins of attraction of these equilibrium schooling modes appear to have shrunk. The results for $A = 0.1$ are the most striking, as most of the curves either exhibit collisions or are on the path to collision, and only a few reach the final time $t = 60$ (30 flapping periods).

Taken together, the simulation results shown in [figure 6](#) demonstrate that both as the number n of plates in an in-line formation increases, and as the heaving amplitude A decreases, the basins of attraction of the equilibria shrink, with most of the stability being lost for $A = 0.1$ and $n = 4$. The loss of stability can be attributed to the increasing relative size of the oscillations in d_k observed as n increases and A decreases.

3.5. Stabilisation of schooling modes

To prevent the loss of stability and collisions observed in [figure 6](#), we propose a simple stabilisation algorithm: if the distance decreases (increases) between a given plate and the one directly ahead of it, then slow it down (speed it up) by decreasing (increasing) its flapping amplitude. We implement this mechanism by allowing the heaving amplitude A in (2.4b) to depend on each plate, and evolving the amplitude A^j of plate j according to the rule

$$A^j(t) = A_0[1 + \beta d_j'(t)], \quad (3.3)$$

where A_0 is the initial amplitude, and $d_j' = U^{j-1} - U^j$ is the rate of change of the distance between the plates. The updated values of A^j are entered in step (i) of the numerical method (§ 2.3), where V is replaced by $V_j(t) = A^j(t) \pi \cos(\pi t)$, and thereby affect all remaining steps (ii)–(v) at each time step.

The stabilisation parameter β determines how fast the amplitude changes occur as the distance between plates changes. Small values of β may not be sufficient to prevent collisions in finite time. Large values of β lead to fast adjustment, but can also lead to stiffness of the numerical scheme. For all runs shown below, we used $0.15 \leq \beta \leq 5$.

[Figure 7](#) shows the distances d_1 , d_2 and d_3 between each pair of plates for a formation of $n = 4$ wings, computed with the stabilisation mechanism. The figure shows that the stabilisation either eliminates or significantly reduces the oscillations in d_j , which quickly approach a steady state. Apart from the smallest value of d_0 (black curves), all of the collisions observed in [figure 6](#) are avoided, with steady-state solutions approached even in the most unstable case, $n = 4$ and $A = 0.1$. We note that d_1 is not shown with $n = 2$, nor d_2 with $n = 3$, since in the absence of collisions, the results are the same as with $n = 4$. For the sake of clarity, the curves in [figure 7](#) are colour-coded by the equilibrium state that they reach, as opposed to the equilibrium state reached by the corresponding wing pair ($n = 2$) in [figure 6](#). Supplementary movie 4 contains examples of simulations with

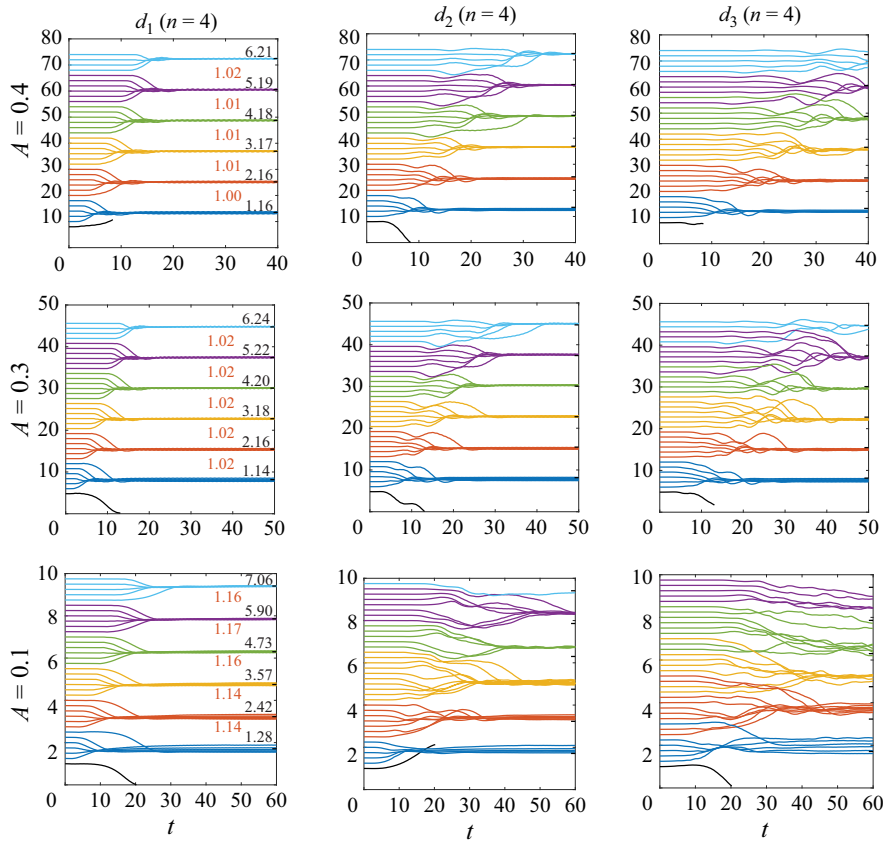


Figure 7. Same as figure 6, but with the stabilisation rule (3.3) and $n = 4$ throughout. The stabilisation factors are $\beta = 0.15, 0.4$ and 5.0 for the flapping amplitudes $A = 0.4, 0.3$ and 0.1 , respectively. Here, the curves are colour-coded simply by the equilibrium state that they reach.

$n = 3$ plates, and shows how the stabilisation algorithm prevents a collision between the two trailing plates.

The stabilisation has a significant impact on the vortex wake behind the plates, as an equilibrium state is reached more quickly. In figure 8, we compare snapshots of the vortex sheet behind two plates without (figure 8a) and with (figure 8b) stabilisation. Figure 8(a) is the same as shown earlier in figure 3(b), but at a different scale. The formation of a wake of quadrupoles is seen early on (near the plates) in figure 8(a), but no clear pattern emerges far from the plates. On the other hand, the results obtained with stabilisation (figure 8b) clearly show the emergence of a stable pattern of quadrupoles behind the plates. A positive (negative) vortex is created behind each plate by the plate's upward (downward) motion. With stabilisation, these four vortices per oscillation period are positioned in a regular stable configuration, which grows slightly in time and space as the plates move forward. Figure 9 shows the vorticity in the wake, corresponding to the regularised vortex sheet shown in figure 8. Figure 9(b) clearly shows the stable pattern in the wake, growing in time and space. The contrast with figure 9(a), which shows much less organised wake vorticity without any growth, is striking.

Figure 10 shows the vorticity in the wake of $n = 3$ plates, with and without stabilisation. Here, each heaving cycle of the three plates generates six vortices per period. Without stabilisation (figure 10a), the vortices exhibit a coherent pattern only at short times

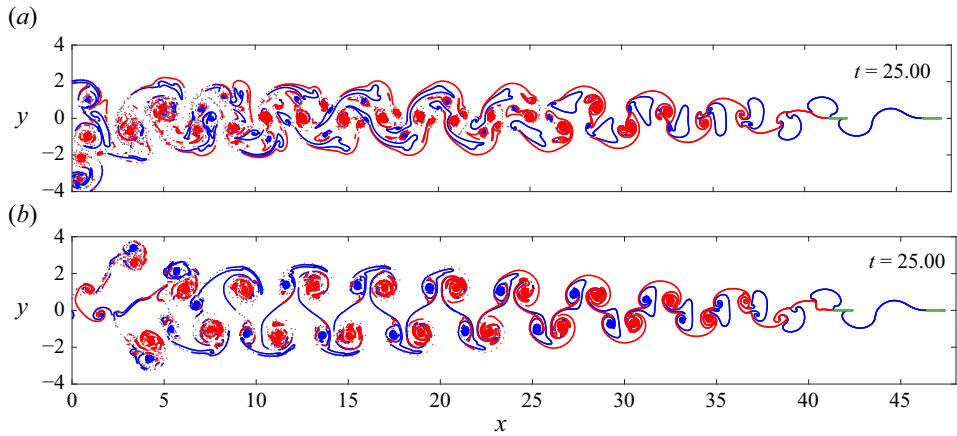


Figure 8. Wake at $t = 25$ behind a pair of plates ($n = 2$) with heaving amplitude $A_0 = 0.2$ and initial separation distance $d_0 = 4.2$. The plots are (a) without stabilisation, and (b) stabilised according to (3.3) with $\beta = 2$.

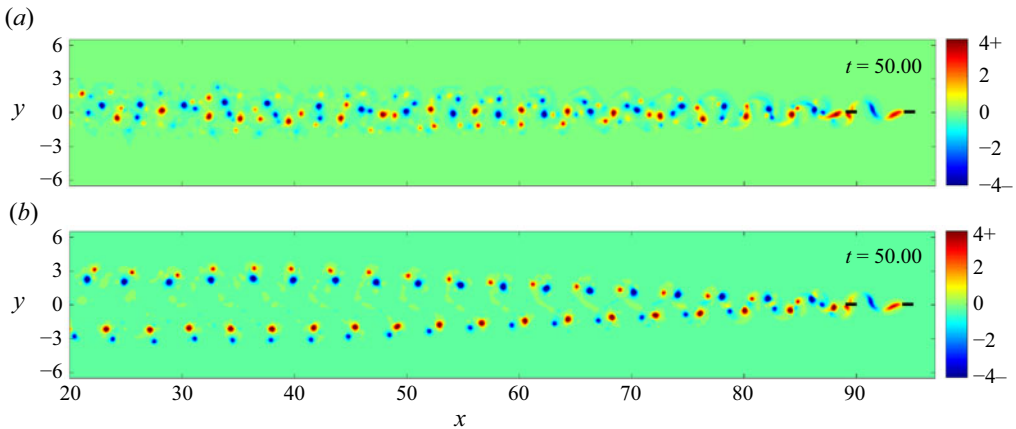


Figure 9. Vorticity at $t = 50$, with the same parameters as in figure 8.

after separation, but they become less organised further downstream. By contrast, with stabilisation (figure 10b), a regular configuration of six vortices per period clearly emerges. The width of the wake grows in time and space, as was the case for a pair of plates ($n = 2$, figure 9b).

We were unable to compute such stable patterns of eight vortices per period in the wake of $n = 4$ plates due to the computational cost of doing so. While the stabilisation mechanism allows stable schooling modes to be achieved relatively quickly, the vortex configurations take longer to reach equilibrium. Long time simulations using fast tree-algorithms (Greengard & Rokhlin 1987; Wang, Krasny & Tlupova 2020) can be performed in the future to study this phenomenon further.

3.6. Reduced model based on thin-aerofoil theory

We now propose and analyse a reduced model to provide rationale for two of the phenomena observed in our simulations (§ 3.4), namely, that collectives of heaving plates in an in-line formation are increasingly stabilised as the flapping amplitude is increased

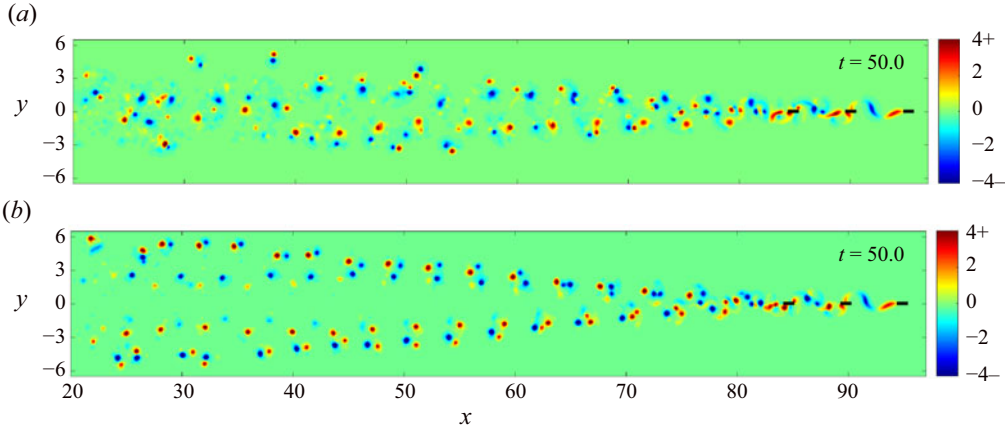


Figure 10. Vorticity at $t = 50$ behind three plates ($n = 3$) with heaving amplitude $A_0 = 0.2$ and initial separation distance $d_0 = 4.2$. The plots are (a) without stabilisation, and (b) stabilised according to (3.3) with $\beta = 2$.

progressively, and such collectives become less stable as the number of plates increases. To that end, we deploy the seminal thin-aerofoil theory of Wu (1961), who considered the motion of a single flat plate executing a small amplitude heaving motion ($A \ll 1$) while translating horizontally at velocity U in an inviscid and incompressible two-dimensional fluid. To simplify the problem, the plate is assumed to shed a flat vortex sheet from its trailing edge, and the sheet strength is determined by the Kutta condition. By solving the linearised Euler equations using conformal mapping, the (dimensionless) thrust T_0 on the plate is found to be

$$T_0 = \frac{\pi}{2} (\pi A)^2 |C(\sigma)|^2, \quad (3.4)$$

where

$$C(\sigma) = \frac{K_1(i\sigma)}{K_0(i\sigma) + K_1(i\sigma)} \quad (3.5)$$

is the so-called Theodorsen function, $K_{0,1}$ are the modified Bessel functions of the second kind of orders zero and one, and $\sigma = \pi/(2U)$ is the reduced frequency. An analogous theory has been developed to describe how a follower plate located downstream of the leader and executing the same heaving kinematics would be affected by the leader's wake (Wu & Chwang 1975; Ramanarivo *et al.* 2016). In this theory, the no-penetration boundary condition is not satisfied simultaneously on both wings; instead, an approximation for the hydrodynamic thrust on the follower is found by assuming that the leader's wake is unaffected by the follower's presence. This assumption is consistent with our numerical simulations before the leader's wake has reached the follower, as discussed in § 3.2. This thrust is found to be $T = T_0[1 + F(d)]$, where d is the distance between the leader's trailing edge and the follower's leading edge (as in figure 1), and

$$F(d) = G(\sigma)^2 + 2G(\sigma) \cos \left[2\pi \left(\frac{d}{2U} - g(\sigma) + \frac{\sigma}{\pi} \right) \right]. \quad (3.6)$$

Here, the real-valued functions $G(\sigma)$ and $g(\sigma)$ are defined through the relation

$$G(\sigma) e^{2\pi i g(\sigma)} = \frac{K_1(-i\sigma) K_0(i\sigma) + K_0(-i\sigma) K_1(i\sigma)}{K_1(i\sigma) [K_0(i\sigma) + K_1(i\sigma)]}. \quad (3.7)$$

A	Simulations	Thin-aerofoil theory
0.1	0.665	0.544
0.2	1.85	1.506
0.3	3.584	3.006
0.4	5.826	5.147

Table 1. The values of the velocity U of a single wing, as obtained in our vortex sheet simulations (§ 3.1) and predicted by thin-aerofoil theory from (3.9), are shown for different values of the flapping amplitude A .

We thus propose the following model for a collective of n plates that execute small-amplitude heaving kinematics in an in-line formation:

$$\begin{aligned} M\ddot{x}_1 + C_d\dot{x}_1^{3/2} &= T_0, \\ M\ddot{x}_m + C_d\dot{x}_m^{3/2} &= T_0 [1 + F(x_{m-1} - x_m - 1)], \quad 2 \leq m \leq n, \end{aligned} \quad (3.8)$$

where x_m is the horizontal position of the centre of the m th plate. We have assumed that each plate is influenced only by its nearest upstream neighbour; that is, the leader wing (x_1) is unaffected by all of the followers, and moves at a steady speed U determined by the balance between drag and thrust forces on it:

$$C_d U^{3/2} = \frac{\pi}{2} (\pi A)^2 |C(\sigma)|^2. \quad (3.9)$$

Every other wing is influenced by its upstream neighbour through the function F , which depends on the steady speed U . That is, our theory is valid in the quasi-steady regime in which the wings' velocities are all close to U . The nearest-neighbour assumption may be justified using our simulations that employ stabilisation (figure 7); specifically, $d_1^{\infty,k} \approx d_2^{\infty,k} \approx d_3^{\infty,k}$, which suggests that the equilibrium distances are mostly insensitive to the number of upstream wings. The assumption is also supported by recent experiments on up to five flapping hydrofoils in an in-line formation (Newbolt *et al.* 2024). Table 1 shows a comparison between the steady speeds U obtained in our vortex sheet simulations and those predicted from (3.9), with surprisingly good agreement given the simplified nature of our reduced model.

We proceed by seeking steadily translating solutions of (3.8), in which the wings move at a constant speed U with a constant separation distance d between them, $x_m(t) - x_{m+1}(t) = d + 1$. By substituting the form $x_m(t) = Ut - (m - 1)(d + 1)$ into (3.8), we find that d satisfies the algebraic equation

$$F(d) = 0. \quad (3.10)$$

This equation has infinitely many positive solutions $d^{\infty,k}$ for $k \in \mathbb{Z}_{>0}$. For the parameter values adopted in this paper, $M = 1$, $C_d = 0.1$ and $A = 0.1$ – 0.4 , we find that the corresponding schooling numbers $S_k = d^{\infty,k}/(2U)$ are equal to $S_1 + k - 1$, where S_1 is between 0.95 and 1.1, in good agreement with values obtained in our vortex sheet simulations (figure 6). We note that a similar result was obtained for two plates by Ramanananarivo *et al.* (2016) using a similar thin-aerofoil theory, and by Baddoo *et al.* (2023) using a more sophisticated thin-aerofoil theory based on conformal maps of multiply connected domains. Reduced models of flapping wings that approximate the hydrodynamic interactions using time-delay differential equations also recover near-integer values of the equilibrium schooling numbers (Heydari, Hang & Kanso 2024; Newbolt *et al.* 2024). We also note that (3.10) is satisfied by a second family of solutions

with schooling numbers $\tilde{S}_k = \tilde{S}_1 + k - 1$, where \tilde{S}_1 is between 0.6 and 0.7 for the parameter values adopted in this paper. We neglect these solutions in the forthcoming discussion because they are linearly unstable to perturbations and thus not observed in our simulations or in laboratory experiments (Ramanarivo *et al.* 2016).

We now examine the linear stability of the state in which the distance between each pair of wings corresponds to the schooling number S_1 , the analysis of the other schooling numbers S_k being identical due to the periodicity of the function F . To that end, we substitute the form $x_m(t) = Ut - (m - 1)(d^{\infty,1} + 1) + \epsilon \tilde{x}_m(t)$ into (3.8), and retain terms at leading order in ϵ . The linearised equations are thus (dropping the tildes)

$$\begin{aligned} M\ddot{x}_1 + \frac{3C_d}{2}U^{1/2}\dot{x}_1 &= 0, \\ M\ddot{x}_m + \frac{3C_d}{2}U^{1/2}\dot{x}_m &= T_0\xi(x_{m-1} - x_m), \quad 2 \leq m \leq n, \end{aligned} \quad (3.11)$$

where $\xi = F'(d^{\infty,1})$. We assume that an impulsive perturbation is applied to the leader:

$$x_1(0) = 1, \quad \dot{x}_1(0) = s_1 \equiv -\frac{3C_d U^{1/2}}{2M} \quad \text{and} \quad x_m(0) = \dot{x}_m(0) = 0 \text{ for } m \geq 2. \quad (3.12)$$

It is straightforward to obtain the solutions

$$\begin{aligned} x_1(t) &= e^{s_1 t} \quad \text{and} \quad x_2(t) = e^{s_1 t} + \text{Re}[B_0^{(2)} e^{s_2 t}], \quad \text{where} \quad B_0^{(2)} = -1 + \frac{is_1}{2\omega}, \\ \omega &= \frac{|s_1|}{2} \sqrt{\frac{16MU^{1/2}\xi}{9C_d} - 1} \quad \text{and} \quad s_2 = \frac{s_1}{2} + i\omega \end{aligned} \quad (3.13)$$

is a root of the quadratic polynomial $p(s) \equiv Ms^2 + (3C_d/2)U^{1/2}s + T_0\xi$. We find that $\omega \in \mathbb{R}$ for the parameter values adopted in this paper. Each wing after the second oscillates in resonance with its upstream neighbour, so the general solution to (3.11) has the form

$$x_m(t) = e^{s_1 t} + \text{Re} \left[\sum_{k=0}^{m-2} B_k^{(m)} t^k e^{s_2 t} \right]. \quad (3.14)$$

The coefficients $B_0^{(m)}$ may be obtained using the initial conditions:

$$B_0^{(m)} = -1 + \frac{i}{\omega} \left(\frac{s_1}{2} + \text{Re} [B_1^{(m)}] \right), \quad m \geq 3. \quad (3.15)$$

To obtain the remaining coefficients, we write (3.11) in the compact form $\mathcal{L}x_m = T_0\xi x_{m-1}$ for $m \geq 2$, where $\mathcal{L} = p(d/dt)$. Using the facts that

$$\begin{aligned} \mathcal{L} e^{s_1 t} &= T_0\xi e^{s_1 t}, \quad \mathcal{L} e^{s_2 t} = 0, \quad \mathcal{L} t e^{s_2 t} = 2i\omega M e^{s_2 t} \\ \text{and} \quad \mathcal{L} t^k e^{s_2 t} &= \left[2i\omega M k t^{k-1} + M k(k-1) t^{k-2} \right] e^{s_2 t} \quad \text{for } k \geq 2, \end{aligned} \quad (3.16)$$

it can be shown that the coefficients $B_k^{(m)}$ satisfy the recursion relation

$$B_{m-2}^{(m)} = -\frac{iT_0\xi B_{m-3}^{(m-1)}}{2\omega M(m-2)} \quad \text{for } m \geq 4, \quad (3.17a)$$

$$2i\omega MB_{k+1}^{(m)}(k+1) + MB_{k+2}^{(m)}(k+1)(k+2) = T_0\xi B_k^{(m-1)} \quad \text{for } k = 0, \dots, m-4. \quad (3.17b)$$

Taken together, (3.15) and (3.17) determine all of the coefficients in the solution (3.14).

We proceed by making two observations about this solution. First, the equilibrium schooling states are linearly stable because the perturbations decay in time, $x_m(t) \rightarrow 0$ as $t \rightarrow \infty$. Moreover, the decay rate $s_1/2$ increases with U , as is evident from (3.12), and thus with the flapping amplitude A , providing a rationale for the observation from our vortex sheet simulations (§ 3.4) that a larger flapping amplitude stabilises the schooling state. Second, by plotting the solution (3.14) for the parameter values adopted in this paper, we observe that the perturbations are amplified downstream, in that at intermediate times they exhibit oscillations that grow in time and have progressively larger amplitude as m increases. To see why this is the case, we observe that the exponential decay factors $e^{s_2 t}$ in (3.14) are multiplied by increasingly large powers of t as m increases. More precisely, note that (3.17a) can be solved explicitly for $B_{m-2}^{(m)}$, from which the long-time asymptotic behaviour of $x_m(t)$ can be deduced:

$$x_m(t) \sim \text{Re}[X_m(t)] \text{ as } t \rightarrow \infty, \quad \text{where } X_m(t) = \frac{B_0^{(2)}}{(m-2)!} \left(\frac{-iT_0\xi}{2\omega M} \right)^{m-2} t^{m-2} e^{s_2 t}. \quad (3.18)$$

We find that for the parameter values adopted in this paper, $|X_m(t)|$ provides an adequate approximation for the envelope of the oscillating solution $x_m(t)$ in (3.14). Moreover, it is easy to see that $|X_m(t)| \propto t^{m-2} e^{s_1 t/2}$ attains its maximum value

$$X_m^* \equiv |X_m(t_m)| = \frac{|B_0^{(2)}|}{(m-2)!} \left(\frac{T_0\xi(m-2)}{\omega M|s_1|e} \right)^{m-2} \quad \text{at the time } t = t_m \equiv \frac{2(m-2)}{|s_1|}. \quad (3.19)$$

By using Stirling's formula, $m! \sim \sqrt{2\pi m} (m/e)^m$ as $m \rightarrow \infty$, we conclude that the peak of the envelope X_m^* increases with m for sufficiently large m provided that $T_0\xi/(\omega M|s_1|) > 1$, as is the case for the parameter values adopted in this paper. Moreover, the time t_m at which the peak is attained increases with m , which further illustrates that the oscillations propagate downstream. The linear theory thus provides a qualitative rationale for the observation from our vortex sheet simulations (§ 3.4) that the schooling states become less stable as the number of wings increases.

While the foregoing linear theory predicts that small-amplitude perturbations to the equilibrium schooling state eventually decay in time, we find that transient linear growth combined with nonlinear effects can cause finite-amplitude perturbations to dislodge the trailing plates from their equilibrium positions. Specifically, we performed numerical simulations of the nonlinear reduced model (3.8), initialising the plates with the positions $x_m(0) = -(m-1)(d^{\infty,1} + 1)$ and velocities $\dot{x}_m(0) = U$ for $m > 1$ and $\dot{x}_1(0) = 1.3U$; that is, we assume that the trailing wings initially move with the steady speed of a single wing, as determined by (3.9), and subject the leader to a finite-amplitude velocity perturbation. The results are shown in figure 11. The middle panel shows the inter-plate distances d_i for $n = 3$ wings and flapping amplitude $A = 0.3$: after a transient, the trailing wings eventually settle back into their equilibrium positions. By contrast, increasing the number of wings to $n = 4$ (right-hand panel) or decreasing the flapping amplitude to $A = 0.2$ (left-hand panel) causes the trailing wings to become dislodged from their equilibrium positions and collide. A qualitatively similar behaviour is observed

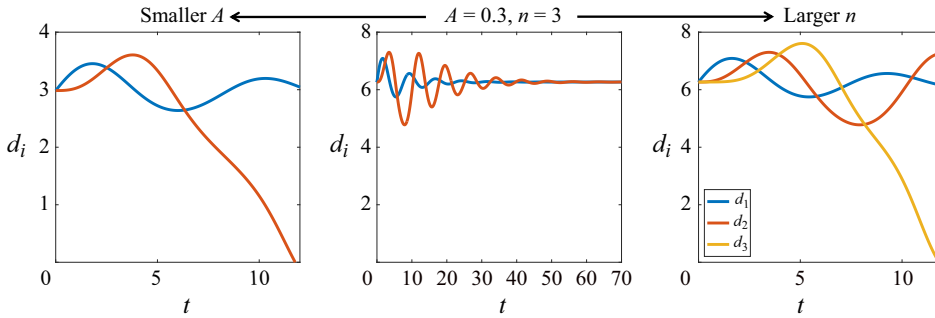


Figure 11. Results of numerical simulations of the (nonlinear) reduced model (3.8). The initial velocity of the leader is $1.3U$, and the remaining plates are initialised in an equilibrium schooling mode with velocity U (given by (3.9)) and inter-plate distance $d^{\infty,1}$ (given by (3.10)). The middle panel shows the inter-plate distances for $n = 3$ wings flapping with amplitude $A = 0.3$; after a transient, the system returns to the equilibrium schooling state. The right-hand panel shows the effect of adding a plate ($A = 0.3, n = 4$), and the left-hand panel shows the effect of decreasing the flapping amplitude ($A = 0.2, n = 3$). It is evident that both lead to a collision between the trailing plates.

for the other flapping amplitudes considered in this paper. We thus conclude that despite its simplifications, the reduced model presented in this section captures the two salient features of our vortex sheet simulations, namely, that schooling modes become progressively less stable as the number of wings is increased or the flapping amplitude is decreased.

We note that a number of physical effects are neglected in our reduced model (3.8) for the sake of analytical simplicity. Specifically, the assumptions are that the wake shed by each plate is flat and unaffected by modulations in the plate's horizontal speed, both of which are at odds with our vortex sheet simulations. The model also assumes nearest-upstream-neighbour interactions; while our simulation results seem to confirm this assumption (§ 3.2), strictly speaking each plate feels the vortex sheets shed by all of the other plates.

4. Conclusion

In this paper, we have used a vortex sheet method to simulate the dynamics of n flat plates in a two-dimensional inviscid and incompressible fluid. The plates are in an inline formation and execute a heaving kinematics with amplitude A and frequency f (figure 1), but their horizontal velocities are determined by the balance of hydrodynamic thrust and drag forces. The thrust forces are induced by the vortex sheet strength at the leading edge, which in turn is induced by the prescribed vertical motion and the fluid vorticity. The drag forces depend on the plate velocity and are modelled using a simple $3/2$ power law. Particular care is taken to evaluate the near-singular integrals that arise when a vortex sheet is near a plate, which is required both to ensure that the vortex sheet does not cross the plate and to accurately compute the hydrodynamic thrust on the plate.

We find that the long-time motion of a single plate is independent of the imposed initial velocity U_0 (figure 2). The plate moves forward in an oscillatory manner due to the oscillatory leading edge sheet strength, and leaves a wake of positive and negative vortices, one of each being formed during one oscillation period (figure 4a). The wake of n plates consists of $2n$ vortices generated in each oscillation period, which interact and form a quasi-periodic pattern with wavelength U_{∞}/f (figures 4b–d).

Our simulations show that plates in the wake of prior ones move towards certain equilibrium positions (figure 5). These equilibria are quantised on the schooling number (Becker *et al.* 2015): that is, the distance between a given plate and the one in front of it is approximately an integer multiple of the wavelength U_∞/f . This observation is consistent with prior experiments and vortex sheet simulations of both pairs (Fang 2016; Ramanananarivo *et al.* 2016; Heydari & Kanso 2021) and larger collectives (Newbolt *et al.* 2022, 2024; Heydari, Hang & Kanso 2024) of flapping wings. By varying the initial distance d_0 between each plate and its upstream neighbour, we find the first six equilibrium positions for $n = 2, 3$ and 4 plates, for the three dimensionless flapping amplitudes $A = 0.1, 0.3$ and 0.4 (figure 6). Which equilibrium is approached by a trailing plate depends on its initial distance from the preceding one.

As more plates are added to the formation, they experience increasingly large oscillations in their horizontal motion. This is apparent, for instance, by comparing the three panels in the top row of figure 6, for which the flapping amplitude is $A = 0.4$. The basins of attraction of the equilibrium positions evidently shrink, as evidenced by the trajectories that depart from the equilibria altogether. For smaller values of the flapping amplitude, the in-line formation becomes increasingly unstable, with a number of cases in which the plates not only leave their nearest equilibria but collide with their upstream neighbours. The loss of stability and associated collisions are far more prevalent both as the number of plates n increases and as the amplitude A decreases. For example, for $A = 0.1, n = 4$, less than a third of the initial conditions tested have not collided after thirty flapping periods.

We find that a simple algorithm is sufficient to mitigate the flow-induced instability that we observe: specifically, if a plate approaches (separates from) its upstream neighbour, then it slows down (speeds up) by adjusting its flapping amplitude A . This leads to out-of-sync oscillations until an equilibrium position is reached (figure 7). The stabilised vortex wakes form beautiful organised vortex patterns that are not observed without stabilisation (figures 9 and 10). The stabilised wakes are expected to represent the long-time limit of unstabilised wakes that have not lost stability and reached an equilibrium. The cost of such long-time computations is prohibitive, and the stabilisation scheme enables us compute these patterns in reasonable time, at least for $n = 2$ and 3.

We have also developed a reduced model for the dynamics of hydrodynamically interacting plates based on linear thin-aerofoil theory (Wu 1961; Wu & Chwang 1975; Ramanananarivo *et al.* 2016). In this model, we assume that each plate interacts only with its nearest upstream neighbour, and that each plate sheds a flat vortex sheet that is unperturbed by the other plates. The model is able to recover a number of phenomena observed in our simulations, namely, the quantisation of stable equilibria on the schooling number, the dependence of the translation velocity on the flapping amplitude, and the decreasing stability of the formation as A decreases and n increases.

The flow-induced oscillatory instability and subsequent collisions within increasingly large in-line formations are reminiscent of the ‘flonons’ observed in recent experiments on flapping wings in a water tank by Newbolt *et al.* (2024). These authors posited that the formation destabilised via a resonance cascade, a physical picture that is consistent with our reduced model in § 3.6. Such an instability was not observed in the vortex sheet simulations of in-line formations of pitching plates conducted by Heydari, Hang & Kanso (2024), who instead observed that formations typically destabilised via a loss of cohesion in which trailing plates could not keep up with the rest of the school, and fell behind. We note that one difference between our vortex sheet algorithm and that of Heydari, Hang & Kanso (2024) is that in the latter, the point vortices shed by the plates are manually removed from the fluid after a prescribed dissipation time (Heydari & Kanso

2021). Another difference, which is potentially significant, is that Heydari, Hang & Kanso (2024) consider plates that undergo pitching oscillations about their leading edges, while our plates undergo heaving oscillations. As a consequence, the horizontal force on the plate is generated entirely by the leading-edge suction in our work, while in their work it is dominated by the pressure force normal to the plate (Heydari & Kanso 2021). We also note that we do not observe a ‘compact’ formation in which the plates are separated by less than a chord length, which has been observed in two-dimensional Navier–Stokes simulations of elastic filaments (Zhu *et al.* 2014) and wings (Lin *et al.* 2020) in flows with $Re = O(100)$, and also in three-dimensional Navier–Stokes simulations of flexible plates (Arranz *et al.* 2022).

The in-line formation considered herein may be viewed as a minimal model for a fish school, in which only hydrodynamic interactions are considered at the expense of behavioural rules and sensing. Our results suggest that fish may need to employ active control mechanisms to mitigate the flow-induced instability experienced by increasingly large formations, but that relatively simple control mechanisms (like the one proposed in § 3.5) could be sufficient. A worthwhile future direction would be to consider more sophisticated control mechanisms, such as those based on reinforcement learning (Novati *et al.* 2017; Verma, Novati & Koumoutsakos 2018). One could also explore biologically relevant control mechanisms, such as those inspired by the fish lateral line system, which detects the nearby flow velocity and pressure gradients, and is thought to play an important role in mediating schooling behaviour (Faucher *et al.* 2010; Mekdara *et al.* 2021). While our study was focused on the formation’s streamwise stability, another future direction would be to allow the plates to translate in both the streamwise and lateral directions, and thus examine the two-dimensional stability of various formations, as has been done using models (Gazzola *et al.* 2016), Navier–Stokes simulations (Gazzola *et al.* 2011; Lin *et al.* 2021, 2022) and experiments (Ormonde *et al.* 2023). Moreover, the simulation framework presented herein could be extended straightforwardly to model more complex formations, such as the diamond lattice and so-called ‘phalanx’ formations exhibited by some fish species (Newlands & Porcelli 2008; Ashraf *et al.* 2016, 2017).

Supplementary movies. Supplementary movies are available at <https://doi.org/10.1017/jfm.2025.10215>.

Funding. Support is acknowledged from NSF DMS-2108839 (A.U.O.) and NSF DMS-1909407 (M.S.).

Declaration of interests. The authors report no conflict of interest.

Data availability statement. The data that support the findings of this study are available upon request.

Appendix A. Derivation of the leading-edge thrust

We provide a simple derivation of the thrust or ‘suction’ force on the leading edge of a wing in a general time-dependent flow. The expression can also be found by combining equations (4.62) and (6.89) from Eldredge (2019).

We assume that at a fixed time t , an isolated wing (i.e. a flat plate) is located on the x -axis. For the sake of analytical convenience, we adopt the convention that the plate’s leading edge is at $x = 0$, and its trailing edge is at $x = 1$, so that the plate moves to the left, which is opposite to the convention used in the main text. Let the plate be parametrised in terms of an arc length variable $0 \leq s \leq 1$ by $\mathbf{x}(s) = (s, 0)$, and assume that it has bound vortex sheet strength $\gamma(s)$ (we omit representing the dependence on time, with the understanding that all quantities are time-dependent). Let $\tilde{\gamma}(s) = \gamma(s)\sqrt{s(1-s)}$ be a desingularised vortex sheet strength, which is assumed to be a regular function of s (Eldredge 2019, p. 120). The fluid velocity induced by the vorticity is given by the

Birkhoff–Rott integral

$$\mathbf{u}(x, y) = \frac{1}{2\pi} \int_0^1 \frac{(-y, x-s)}{(x-s)^2 + y^2} \frac{\tilde{\gamma}(s)}{\sqrt{(1-s)s}} ds + \mathbf{w}, \quad (\text{A1})$$

where \mathbf{w} is a smooth velocity due to free and other bound vorticity in the fluid.

Following Saffman (1995, p. 98), the suction force is calculated by integrating the Euler momentum equation in a small disk B_ϵ of radius $\epsilon \ll 1$ about the leading edge $(x, y) = (0, 0)$:

$$\frac{\partial}{\partial t} \int_{B_\epsilon} \mathbf{u} dV + \int_{S_\epsilon} [p \mathbf{n} + \mathbf{u}(\mathbf{u} \cdot \mathbf{n})] dS = \int_{B_\epsilon} \mathbf{F} dV \quad (\text{A2})$$

$$= -T \hat{\mathbf{i}}, \quad (\text{A3})$$

where p is the pressure, \mathbf{n} is the outward unit normal to the surface S_ϵ of B_ϵ , and $\mathbf{F} = -T \delta(\mathbf{x}) \hat{\mathbf{i}}$ is the external force, i.e. the force that the leading edge of the wing exerts on the fluid. The suction force of the fluid on the wing is then $T \hat{\mathbf{i}}$. Here, we have taken the fluid density to be 1. The pressure can be eliminated using Bernoulli's law (Saffman 1995, p. 19)

$$\frac{\partial \phi}{\partial t} + p + \frac{1}{2} |\mathbf{u}|^2 = H(t), \quad (\text{A4})$$

where ϕ is the velocity potential, and $H(t)$ is an arbitrary function of time. Multiply (A4) by \mathbf{n} and take the surface integral over S_ϵ to obtain at leading order

$$\int_{S_\epsilon} p \mathbf{n} dS = -\frac{1}{2} \int_{S_\epsilon} |\mathbf{u}|^2 \mathbf{n} dS, \quad (\text{A5})$$

where we have neglected terms that are less singular at the plate's leading edge and thus give higher-order contributions in ϵ . Substitute (A5) into (A3), and note that the volume integral $(\partial/\partial t) \int_{B_\epsilon} \mathbf{u} dV$ gives a higher-order contribution in ϵ , to obtain

$$T \hat{\mathbf{i}} = \lim_{\epsilon \rightarrow 0} \int_{S_\epsilon} \left[\frac{1}{2} |\mathbf{u}|^2 \mathbf{n} - \mathbf{u}(\mathbf{u} \cdot \mathbf{n}) \right] dS. \quad (\text{A6})$$

We now calculate the velocity at leading order in ϵ for $(x, y) \in B_\epsilon$. In (A1), make the change of variable $-v = x - s$ and expand $\tilde{\gamma}(x+v) = \tilde{\gamma}(x) + \tilde{\gamma}'(x)v + \dots$ to obtain, for $\mathbf{u} = (u_1, u_2)$,

$$\begin{aligned} u_1(x, y) &= -\frac{y}{2\pi} [\tilde{\gamma}(x) W_0(x, y) + \tilde{\gamma}'(x) W_1(x, y)] + O(1), \\ u_2(x, y) &= -\frac{\tilde{\gamma}(x)}{2\pi} W_1(x, y) + O(1), \end{aligned} \quad (\text{A7})$$

where

$$\begin{aligned} W_0(x, y) &= \int_{-x}^{1-x} \frac{1}{(v^2 + y^2) \sqrt{(1-(v+x))(v+x)}} dv, \\ W_1(x, y) &= \int_{-x}^{1-x} \frac{v}{(v^2 + y^2) \sqrt{(1-(v+x))(v+x)}} dv, \end{aligned} \quad (\text{A8})$$

and the $O(1)$ remainder in (A7) refers to terms for which the Birkhoff–Rott kernel is integrable in v as $y \rightarrow 0$. The integrals in (A8) can be evaluated in closed form. Let

$F(x, y) = \sqrt{(1-x)^2 + y^2}$ and $G(x, y) = \sqrt{x^2 + y^2}$. Then (Geer & Keller 1968)

$$\begin{aligned} W_0(x, y) &= \pi (F + G) \left\{ (FG)^2 \left[(F + G)^2 - 1 \right] \right\}^{-1/2}, \\ W_1(x, y) &= \pi (-xF + (1-x)G) \left\{ (FG)^2 \left[(F + G)^2 - 1 \right] \right\}^{-1/2}. \end{aligned} \quad (\text{A9})$$

Evaluation of (A9) for $x = \epsilon \cos \theta$, $y = \epsilon \sin \theta$ on S_ϵ gives, to leading order in ϵ ,

$$\begin{aligned} W_0 &= \frac{\pi}{\sqrt{2(1-\cos \theta)}} \epsilon^{-3/2} + O(\epsilon^{-1/2}), \\ W_1 &= \pi \sqrt{\frac{1-\cos \theta}{2}} \epsilon^{-1/2} + O(\epsilon^{1/2}). \end{aligned} \quad (\text{A10})$$

From (A7) and (A10), the leading-order velocity components on S_ϵ are

$$\begin{aligned} u_1 &= -\frac{\tilde{\gamma}(0)}{2\sqrt{2}} \frac{\sin \theta}{(1-\cos \theta)^{1/2}} \epsilon^{-1/2} + O(1), \\ u_2 &= -\frac{\tilde{\gamma}(0)}{2\sqrt{2}} (1-\cos \theta)^{1/2} \epsilon^{-1/2} + O(1). \end{aligned} \quad (\text{A11})$$

The surface integral in the expression for the suction force can now be computed by substituting (A11) and $\mathbf{n} = (\cos \theta, \sin \theta)$ into (A6). We find that the y -component of the suction force is zero as expected, while the x -component satisfies

$$T\hat{\mathbf{i}} = -\frac{\pi}{4} \tilde{\gamma}^2(0) \hat{\mathbf{i}}. \quad (\text{A12})$$

More generally, the magnitude of the suction force for a horizontal plate with leading edge located at \mathbf{x} is

$$|T| = \frac{\pi}{4} \tilde{\gamma}^2(\mathbf{x}), \quad (\text{A13})$$

with the force oriented in the negative x direction when the leading edge of the wing is located on the left, and in the positive x direction when the leading edge is on the right.

Appendix B. Comparison between unsteady and steady flow around a vertically translating flat plate

A simple argument for steady flow past a plate, as considered by Acheson (1990, p. 153), gives results consistent with those of Appendix A. Consider a plate of length $4a$ placed at $x \in [-2a, 2a]$, aligned horizontally with the x -axis, moving with velocity (U, V) in an inviscid fluid at rest at infinity. Since the horizontal component does not impact thrust, we set $U = 0$. Here, we derive the leading-edge normalised sheet strength and leading-edge suction for steady plate motion with singular flow at the leading edge (at $z = 2a$), and smooth flow satisfying the Kutta condition at the trailing edge (at $z = -2a$). The steady flow in a reference frame moving with the plate is obtained by the conformal map from the unit circle $|\zeta| = a$ onto the plate on the x -axis with $x \in [-2a, 2a]$:

$$z = J(\zeta) = \zeta + \frac{a^2}{\zeta}, \quad \text{with } \zeta = J^{-1}(z) = \frac{1}{2} \left(z + \sqrt{z^2 - 4a^2} \right). \quad (\text{B1})$$

Potential flow around the circle with circulation Γ is given by the complex potential

$$w(\zeta) = iV \left(\zeta - \frac{a^2}{\zeta} \right) - i \frac{\Gamma}{2\pi} \log \zeta. \quad (\text{B2})$$

The complex potential in the z -plane is $W(z) = w(J^{-1}(z))$, with complex velocity

$$\frac{dW}{dz} = \frac{dw/d\zeta}{dz/d\zeta} = iV \left(1 + \frac{a^2}{\zeta^2} - \frac{\Gamma}{2\pi V \zeta} \right) \frac{1}{1 - a^2/\zeta^2} = \frac{iV}{\zeta^2 - a^2} \left(\zeta^2 - \frac{\Gamma}{2\pi V} \zeta + a^2 \right). \quad (\text{B3})$$

The singularity at the trailing edge $z = -2a$ ($\zeta = -a$) is removed by setting

$$\Gamma = -4\pi V a, \quad (\text{B4})$$

so that

$$\frac{dW}{dz} = iV \frac{\zeta + a}{\zeta - a}. \quad (\text{B5})$$

The resulting velocity on the plate is obtained by setting $\zeta = a e^{i\theta}$ ($x = 2a \cos \theta$), where $\theta \in [0, \pi]$ corresponds to the top of the plate, and $\theta \in [\pi, 2\pi]$ to the bottom:

$$\begin{aligned} \frac{dW}{dz} &= V \frac{\sin \theta}{1 - \cos \theta} = V \frac{\pm \sqrt{1 - \cos^2 \theta}}{1 - \cos \theta} = V \frac{\pm \sqrt{1 + \cos \theta}}{\sqrt{1 - \cos \theta}} \\ &= \pm V \frac{\sqrt{2a + x}}{\sqrt{2a - x}} = \pm V \frac{2a + x}{\sqrt{4a^2 - x^2}}. \end{aligned} \quad (\text{B6})$$

For positive V , the top velocity is positive and the bottom is negative. This yields the vortex sheet strength

$$\gamma(x) = u_- - u_+ = -2V \frac{2a + x}{\sqrt{4a^2 - x^2}} = -2V \frac{2a + x}{\sqrt{4a^2 - x^2}} = \frac{\tilde{\gamma}(x)}{\sqrt{4a^2 - x^2}}, \quad (\text{B7})$$

where $\tilde{\gamma}(x) = \gamma(x) \sqrt{4a^2 - x^2}$. This definition of $\tilde{\gamma}$ is consistent with (A1) with $s = x + 1/2$, $a = 1/4$, and (2.6) with $s = x$, $a = 1/4$. For $a = 1/4$, the leading-edge normalised sheet strength is $\tilde{\gamma}(1/2) = -2V$.

Using Blasius' theorem, we find that the total force on the plate is

$$\begin{aligned} F_x - iF_y &= \frac{i\rho}{2} \oint_{C_z} \left(\frac{dW}{dz} \right)^2 dz = \frac{i\rho}{2} \oint_{C_\zeta} \left(\frac{dW}{d\zeta} \right)^2 \frac{dz}{d\zeta} d\zeta \\ &= -V^2 \frac{i\rho}{2} \oint_{C_\zeta} \frac{(\zeta + a)^3}{(\zeta - a)\zeta^2} d\zeta = 4\pi\rho V^2 a = -\rho V \Gamma = \pi\rho a [\tilde{\gamma}(1/2)]^2, \end{aligned} \quad (\text{B8})$$

picking up the residues at $\zeta = 0, a$. Expression (B8) is consistent with (A13) by setting $\rho = 1$, $a = 1/4$.

Figure 12 shows the streamlines of the resulting steady flow past the plate with $V = 1$ and $a = 1/4$, in a reference frame moving with the plate, where the circulation given by (B4) cancels the singularity at the trailing (left-hand) edge. Note the resulting stagnation point at the trailing edge and the symmetry across $y = 0$.

We now consider an impulsively started plate with $a = 1/4$, initially on the x -axis and centred at the origin, moving vertically upwards with constant velocity $V = 1$ for $t > 0$. The singularity at the left-hand edge is resolved by satisfying the Kutta condition through vortex sheet generation and separation via the method described in § 2. Figure 13 shows the position of the plate and the separated vortex sheet at a sequence of times.

Figure 14 shows the corresponding streamlines, in a reference frame moving with the plate. It shows that as $t \rightarrow \infty$, the flow approaches the steady symmetric potential flow discussed above and shown in figure 12. Furthermore, note the position of the stagnation point on the upper plate side. Initially, the impulsively started flow is symmetric, with a

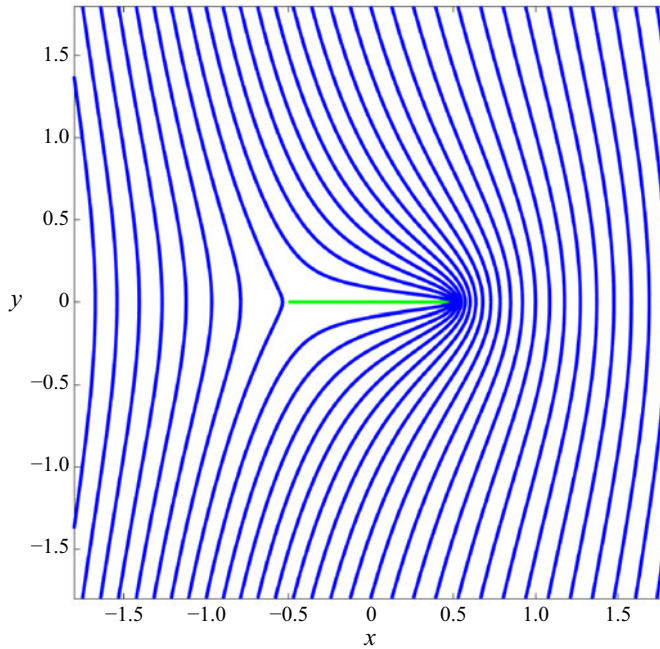


Figure 12. Potential flow past a plate of unit length translating vertically with velocity V , as obtained from (B2) and (B4). The circulation around the plate is $\Gamma = -\pi V$, which cancels the singularity at the left-hand edge.

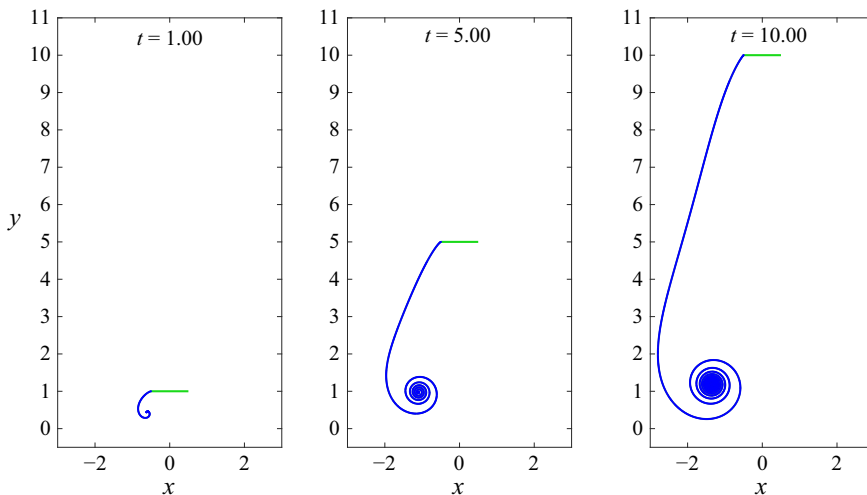


Figure 13. Impulsively started plate that translates vertically with constant velocity $V = 1$, and the vortex sheet that separates from its left-hand endpoint, shown at the indicated times.

stagnation point at the middle of the plate at $x = 0$. As time evolves, the unsteady flow approaches the steady flow configuration, and the stagnation point moves progressively closer to the trailing edge.

Figure 15 shows the desingularised leading-edge sheet strength and the circulation about the plate for the impulsively started plate. Note that the total circulation about the plate and

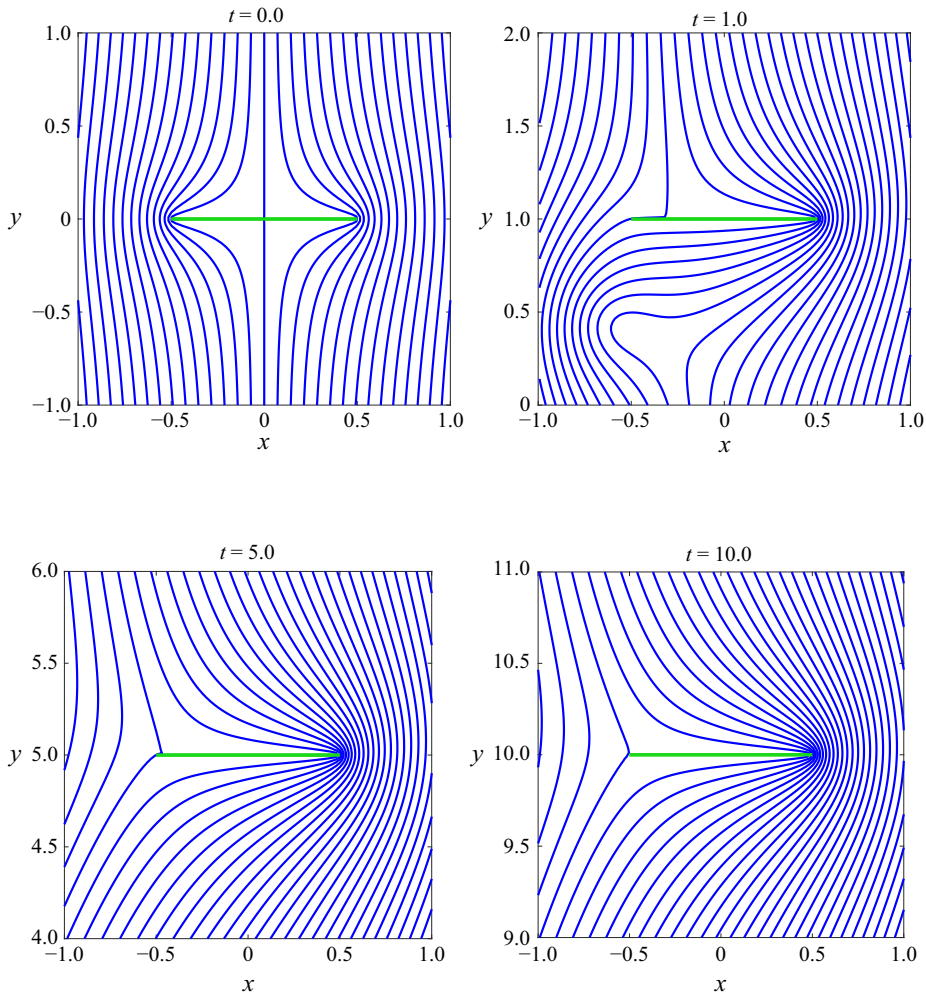


Figure 14. Streamlines of the flow in [figure 13](#), shown in a reference frame moving with the plate.

the shed vortex sheet is enforced to stay constant at zero. The plate circulation is thus the negative of the circulation in the shed vortex sheet. The figure shows that both the shed sheet strength and the plate circulation approach the steady-state values as $t \rightarrow \infty$, with $\tilde{\gamma} \rightarrow -2V$ and $\Gamma \rightarrow -\pi V$.

These numerical results illustrate the difference between steady and unsteady flow, and provide further consistency between the steady-state results derived here and the unsteady results derived in [Appendix A](#).

Appendix C. Alternative model for the drag force acting on the plates

To compute the drag on plate j , we simply use the plate velocity U^j , which induces drag relative to the stagnant background flow. An alternative model that better accounts for the horizontal velocity above and below the plate, used by Fang (2016) and Heydari & Kanso (2021), is obtained by replacing

$$C_d(U^j)^{3/2} \quad (\text{C1})$$

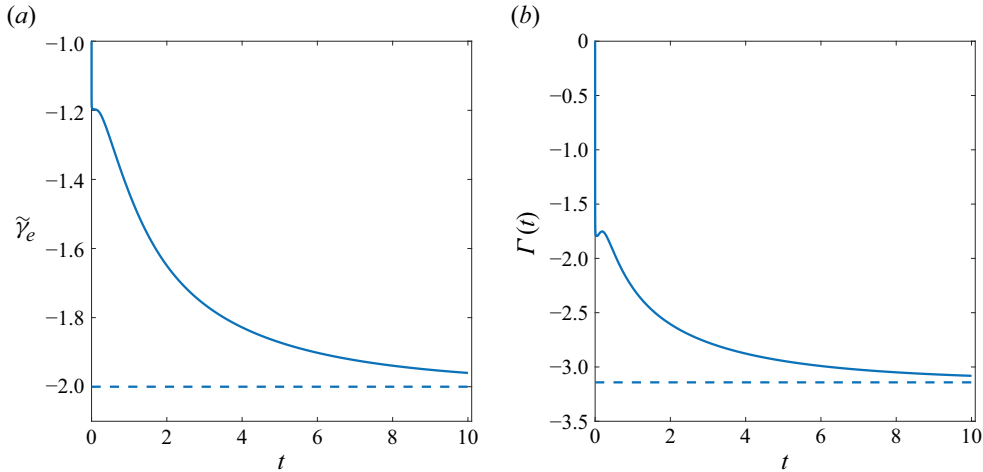


Figure 15. (a) Desingularised leading-edge sheet strength $\tilde{\gamma}(1/2)$, and (b) total circulation around the plate $\Gamma(t)$, corresponding to the flow in figure 13.

in (2.11b) by

$$\frac{C_d}{2} [(U^j - \bar{u}_+^j)^{3/2} + (U^j - \bar{u}_-^j)^{3/2}], \quad (\text{C2})$$

where

$$\bar{u}_\pm^j = \int_0^1 u_\pm^j(s, t) \, ds \quad (\text{C3})$$

are the average horizontal velocities just above and below the plate, and $u_\pm^j(s, t)$ are the limiting horizontal velocities from above and below the plate, respectively. Equation (C2) assumes that $U^j - \bar{u}_\pm^j > 0$, which is the case in the present paper.

The velocities $u_\pm^j(s)$ have two components, one stemming from the j th plate, and one stemming from the far-field vorticity in all the other $n - 1$ plates and all the n wakes:

$$u_\pm^j = u_{\pm \text{plate}}^j + u_{\text{far}}^j. \quad (\text{C4})$$

The average of this sum is the sum of the average of each component.

The first component is discontinuous across the plate. Note that the jump in the horizontal velocity across the plate equals the negative sheet strength, and the average of the horizontal velocities above and below the plate, induced by itself, is zero:

$$u_{+ \text{plate}}^j - u_{- \text{plate}}^j = -\gamma(s, t), \quad (\text{C5a})$$

$$\frac{1}{2} (u_{+ \text{plate}}^j + u_{- \text{plate}}^j) = 0, \quad (\text{C5b})$$

thus

$$u_{+ \text{plate}}^j = -\gamma(s)/2, \quad u_{- \text{plate}}^j = +\gamma(s)/2. \quad (\text{C6})$$

As a result,

$$\bar{u}_{\pm \text{plate}}^j = \mp \frac{1}{2} \int_0^1 \gamma(s) \, ds = \pm \frac{1}{2} \Gamma_T^j. \quad (\text{C7})$$

The last equality follows since the total circulation about each plate is the negative of the shed vorticity Γ_T^j .

Furthermore, note that if $\Gamma_T^j/2 < U^j$, then the contribution of this self-induced term to the difference between (C2) and (C1) is of order

$$C_d \frac{3}{4} \left(\frac{\Gamma_T^j}{2U^j} \right)^2, \quad (\text{C8})$$

so is expected to be small. Indeed, we observe in our simulations that $\Gamma^T/2U \leq 0.4$ for the amplitudes $A = 0.1-0.4$ that we considered, so the contribution (C8) is expected to be $\leq 2\%$ for $C_d = 0.1$.

The second component, the far-field contribution u_{far}^j to $u_{\pm}^j(s, t)$, is continuous across the j th plate. It consists of only the contribution of the free vorticity in all n wakes, and not any bound plate vorticity. The reason the other $n - 1$ plates do not contribute to the horizontal velocity on the j th plate is that they are positioned in line with the j th plate. We compute u_{far}^j by evaluating the horizontal component of

$$\mathbf{u}(\mathbf{x}_o, t) = \frac{1}{2\pi} \sum_{l=1}^n \int_0^{\Gamma_T^l} \frac{(\mathbf{x}_o - \mathbf{x}_f^l(\Gamma, t))^{\perp}}{|\mathbf{x}_o - \mathbf{x}_f^l(\Gamma, t)|^2 + \delta^2} d\Gamma \quad (\text{C9})$$

at all midpoints $\mathbf{x}_o = \mathbf{x}^j(\alpha_k^m)$, then using the midpoint rule to obtain

$$\bar{u}_{\text{far}}^j = \sum_{k=0}^n u(\mathbf{x}^j(\alpha_k^m)) s'(\alpha_k^m) (\alpha_k - \alpha_{k-1}). \quad (\text{C10})$$

This second component is expected to be small for a single plate ($n = 1$), since the wake is behind the plate. It is expected to be less negligible for $n > 1$ plates, when the j th plate is in the wake of the upstream plates.

As a result, we expect the change introduced by the alternative model (C2) over the simple model (C1) to be small if $n = 1$, thus it will not significantly affect the steady-state velocity if $n = 1$. For $n > 1$, the rear plates have been shown to have small impact on the first plate. Since at steady state all plates travel at the same speed, the steady-state velocity for $n > 1$ computed with the alternative model is expected to be similar to that in the original model.

These conjectures were confirmed by numerical results for sample cases using $A = 0.2$ and $C_d = 0.1$. We computed the translation velocity U^j for $n = 1$ and $n = 2$, and the equilibrium separation distance $d_1^{\infty,1}$ for $n = 2$, and found that the translation velocity computed with the alternative drag model decreased by 4 % over the simple model, and the separation distance decreased by 3 %. This shows that there is little difference between the two drag models for the parameter regime considered herein, and changing from one to the other is not expected to change the main conclusions of this paper.

REFERENCES

- ACHESON, D.J. 1990 *Elementary Fluid Dynamics*. Oxford University Press.
- ALBEN, S. 2009 Simulating the dynamics of flexible bodies and vortex sheets. *J. Comput. Phys.* **228** (7), 2587–2603.
- ALBEN, S. 2010 Passive and active bodies in vortex-street wakes. *J. Fluid Mech.* **2642**, 95–125.
- ARRANZ, G., FLORES, O. & GARCÍA-VILLALBA, M. 2022 Flow interaction of three-dimensional self-propelled flexible plates in tandem. *J. Fluid Mech.* **931**, A5.

- ASHRAF, I., BRADSHAW, H., HA, T.-T., HALLOY, J., GODOY-DIANA, R. & THIRIA, B. 2017 Simple phalanx pattern leads to energy saving in cohesive fish schooling. *Proc. Natl Acad. Sci. USA* **114** (36), 9599–9604.
- ASHRAF, I., GODOY-DIANA, R., HALLOY, J., COLLIGNON, B. & THIRIA, B. 2016 Synchronization and collective swimming patterns in fish (*Hemigrammus bleheri*). *J. R. Soc. Interface* **13** (123), 0734.
- BADDOO, P.J., MOORE, N.J., OZA, A.U. & CROWDY, D.G. 2023 Generalization of waving-plate theory to multiple interacting swimmers. *Commun. Pure Appl. Maths* **76** (12), 3811–3851.
- BAJEC, I.L. & HEPPNER, F.H. 2009 Organized flight in birds. *Anim. Behav.* **78** (4), 777–789.
- BECKER, A.D., MASOUD, H., NEWBOLT, J.W., SHELLEY, M. & RISTROPH, L. 2015 Hydrodynamic schooling of flapping swimmers. *Nat. Commun.* **6** (1), 8514.
- DAI, L., HE, G., ZHANG, X. & ZHANG, X. 2018 Stable formations of self-propelled fish-like swimmers induced by hydrodynamic interactions. *J. R. Soc. Interface* **15** (147), 0490.
- ELDRIDGE, J.D. 2019 *Mathematical Modeling of Unsteady Inviscid Flows*. Springer.
- FANG, F. 2016 Hydrodynamic interactions between self-propelled flapping wings. PhD thesis, New York University, USA.
- FANG, F., HO, K.L., RISTROPH, L. & SHELLEY, M.J. 2017 A computational model of the flight dynamics and aerodynamics of a jellyfish-like flying machine. *J. Fluid Mech.* **819**, 621–655.
- FAUCHER, K., PARMENTIER, E., BECCO, C., VANDEWALLE, N. & VANDEWALLE, P. 2010 Fish lateral system is required for accurate control of shoaling behaviour. *Anim. Behav.* **79** (3), 679–687.
- GAZZOLA, M., CHATELAIN, P., VAN REES, W.M. & KOUMOUTSAKOS, P. 2011 Simulations of single and multiple swimmers with non-divergence free deforming geometries. *J. Comput. Phys.* **230** (19), 7093–7114.
- GAZZOLA, M., TCHIEU, A.A., ALEXEEV, D., DE BRAUER, A. & KOUMOUTSAKOS, P. 2016 Learning to school in the presence of hydrodynamic interactions. *J. Fluid Mech.* **789**, 726–749.
- GEDER, J.D., RAMAMURTI, R., EDWARDS, D., YOUNG, T. & PRUESSNER, M. 2017 Development of an unmanned hybrid vehicle using artificial pectoral fins. *Mar. Technol. Soc. J.* **51** (56), 56–70.
- GEER, J.F. & KELLER, J.B. 1968 Uniform asymptotic solutions for potential flow around a thin airfoil and the electrostatic potential about a thin conductor. *SIAM J. Appl. Maths* **16** (1), 75–101.
- GREENGARD, L. & ROKHLIN, V. 1987 A fast algorithm for particle simulations. *J. Comput. Phys.* **73** (2), 325–348.
- GUDGER, E.W. 1944 Fishes that swim heads to tails in single file. *Copeia* **3** (3), 152–154.
- HEYDARI, S., HANG, H., & KANSO, E. 2024 Mapping spatial patterns to energetic benefits in groups of flow-coupled swimmers. *eLife* **13**, RP96129.
- HEYDARI, S. & KANSO, E. 2021 School cohesion, speed and efficiency are modulated by the swimmers flapping motion. *J. Fluid Mech.* **922**, A27.
- HUANG, Y., NITSCHKE, M. & KANSO, E. 2016 Hovering in oscillatory flows. *J. Fluid Mech.* **804**, 531–549.
- JOLLES, J.W., BOOGERT, N.J., SRIDHAR, V.H., COUZIN, I.D. & MANICA, A. 2017 Consistent individual differences drive collective behavior and group functioning of schooling fish. *Curr. Biol.* **27** (18), 2862–2868.
- KRASNY, R. 1986 Desingularization of periodic vortex sheet roll-up. *J. Comput. Phys.* **65** (2), 292–313.
- LI, L., NAGY, M., GRAVING, J.M., BAK-COLEMAN, J., XIE, G. & COUZIN, I.D. 2020 Vortex phase matching as a strategy for schooling in robots and in fish. *Nat. Commun.* **11** (1), 5408.
- LIGHTHILL, J. 1975 *Mathematical Biofluidynamics*. SIAM.
- LIN, X., WU, J., YANG, L. & DONG, H. 2022 Two-dimensional hydrodynamic schooling of two flapping swimmers initially in tandem formation. *J. Fluid Mech.* **941**, A29.
- LIN, X., WU, J., ZHANG, T. & YANG, L. 2020 Self-organization of multiple self-propelling flapping foils: energy saving and increased speed. *J. Fluid Mech.* **884**, R1.
- LIN, X., WU, J., ZHANG, T. & YANG, L. 2021 Flow-mediated organization of two freely flapping swimmers. *J. Fluid Mech.* **912**, A37.
- MEKDARA, P.J., NASIMI, F., SCHWALBE, M.A.B. & TYTELL, E.D. 2021 Tail beat synchronization during schooling requires a functional posterior lateral line system in giant danios, *Devario aequipinnatus*. *Integr. Comp. Biol.* **61** (2), 427–441.
- NEWBOLT, J.W., LEWIS, N., BLEU, M., WU, J., MAVROYIAKOUMOU, C., RAMANANARIVO, S. & RISTROPH, L. 2024 Flow interactions lead to self-organized flight formations disrupted by self-amplifying waves. *Nat. Commun.* **15** (1), 3462.
- NEWBOLT, J.W., ZHANG, J. & RISTROPH, L. 2022 Lateral flow interactions enhance speed and stabilize formations of flapping swimmers. *Phys. Rev. Fluids* **7** (6), L061101.
- NEWLANDS, K. & PORCELLI, T.A. 2008 Measurement of the size, shape and structure of Atlantic bluefin tuna schools in the open ocean. *Fish. Res.* **91** (1), 42–55.
- NITSCHKE, M. 2021 Evaluation of near-singular integrals with application to vortex sheet flow. *Theor. Comput. Fluid Dyn.* **35** (5), 581–608.

- NITSCHKE, M. & KRASNY, R. 1994 A numerical study of vortex ring formation at the edge of a circular tube. *J. Fluid Mech.* **276**, 139–161.
- NOVATI, G., VERMA, S., ALEXEEV, D., ROSSINELLI, D., VAN REES, W.M. & KOUMOUTSAKOS, P. 2017 Synchronisation through learning for two self-propelled swimmers. *Bioinspir. Biomim.* **12** (3), 036001.
- ORMONDE, P.C., KURT, M., MIVEHCHI, A. & MOORED, K.W. 2024 Two-dimensionally stable self-organisation arises in simple schooling swimmers through hydrodynamic interactions. *J. Fluid Mech.* **1000**, A90.
- PARK, S.G. & SUNG, H.J. 2018 Hydrodynamics of flexible fins propelled in tandem, diagonal, triangular and diamond configurations. *J. Fluid Mech.* **840**, 154–189.
- PARTRIDGE, B.L., PITCHER, T., CULLEN, J.M. & WILSON, J. 1980 The three-dimensional structure of fish schools. *Behav. Ecol. Sociobiol.* **6** (4), 277–288.
- PAVLOV, D.S. & KASUMYAN, A.O. 2000 Patterns and mechanisms of schooling behavior in fish: a review. *J. Ichthyol.* **40**, S163–S231.
- PENG, Z.-R., HUANG, H. & LU, X.-Y. 2018 Hydrodynamic schooling of multiple self-propelled flapping plates. *J. Fluid Mech.* **853**, 587–600.
- PITCHER, T.J. 1973 The three-dimensional structure of schools in the minnow, *Phoxinus phoxinus* (L.). *Anim. Behav.* **21** (4), 673–686.
- PORTUGAL, S., HUBEL, T., FRITZ, J., HEESE, S., TROBE, D., VOELKL, B., HAILES, S., WILSON, A.M. & USHERWOOD, J.R. 2014 Upwash exploitation and downwash avoidance by flap phasing in ibis formation flight. *Nature* **505** (7483), 399–402.
- RAMANANARIVO, S., FANG, F., OZA, A., ZHANG, J. & RISTROPH, L. 2016 Flow interactions lead to orderly formations of flapping wings in forward flight. *Phys. Rev. Fluids* **1**, 071201(R).
- SAFFMAN, P.G. 1995 *Vortex Dynamics*. Cambridge University Press.
- SHELLEY, M.J. 1992 A study of singularity formation in vortex-sheet motion by a spectrally accurate vortex method. *J. Fluid Mech.* **244**, 493–526.
- SHENG, J.X., YSASI, A., KOLOMENSKIY, D., KANSO, E., NITSCHKE, M. & SCHNEIDER, K. 2012 Simulating vortex wakes of flapping plates. In *Natural Locomotion in Fluids and on Surfaces* (ed. S. CHILDRESS, A. HOSOI, W.W. SCHULTZ & J. WANG), pp. 255–262. Springer.
- SWAIN, D.T., COUZIN, I.D. & LEONARD, N.E. 2015 Coordinated speed oscillations in schooling killifish enrich social communication. *Curr. Biol.* **25** (5), 1077–1109.
- TRIANTAFYLLOU, M.S., TRIANTAFYLLOU, G.S. & YUE, D.K.P. 2000 Hydrodynamics of fishlike swimming. *Annu. Rev. Fluid Mech.* **32** (1), 33–53.
- TUNSTRØM, K., KATZ, Y., IOANNOU, C.C., HUEPE, C., LUTZ, M.J., COUZIN, I.D. & BEN-JACOB, E. 2013 Collective states, multistability and transitional behavior in schooling fish. *PLoS Comput. Biol.* **9** (2), e1002915.
- VERMA, S., NOVATI, G. & KOUMOUTSAKOS, P. 2018 Efficient collective swimming by harnessing vortices through deep reinforcement learning. *Proc. Natl Acad. Sci. USA* **115** (23), 5849–5854.
- WANG, L., KRASNY, R. & TLUPOVA, S. 2020 A kernel-independent treecode based on barycentric Lagrange interpolation. *Commun. Comput. Phys.* **28** (4), 1415–1436.
- WU, T.Y. 1961 Swimming of a waving plate. *J. Fluid Mech.* **10** (3), 321–344.
- WU, T.Y. & CHWANG, A.T. 1975 Extraction of flow energy by fish and birds in a wavy stream. In *Swimming and Flying in Nature*, pp. 687–702. Springer.
- ZHU, X., HE, G. & ZHANG, X. 2014 Flow-mediated interactions between two self-propelled flapping filaments in tandem configuration. *Phys. Rev. Lett.* **113** (23), 238105.